Impact of weld restraint on the development of distortion and stress during the electron beam welding of a low-alloy steel subject to solid state phase transformation

Y.L. Sun [a,b,*], A.N. Vasileiou [c], E.J. Pickering [d], J. Collins [d], G. Obasi [d], V. Akrivos [a], M.C. Smith [a]

[a] Department of Mechanical, Aerospace and Civil Engineering, School of Engineering, The University of Manchester, Sackville Street, Manchester M13 9PL, UK
[b] Welding Engineering and Laser Processing Centre, School of Aerospace, Transport and Manufacturing, Cranfield University, Cranfield, MK43 0AL, UK
[c] Dalton Nuclear Institute, The University of Manchester, Sackville Street, Manchester M13 9PL, UK
[d] Department of Materials, School of Natural Sciences, The University of Manchester, Sackville Street, Manchester M13 9PL, UK

ABSTRACT

Electron beam (EB) welding has a low tolerance to inter-part gapping distortion and can generate complicated stresses, which pose challenges to weld quality and integrity. This study investigates welding distortion and stresses in an EB welded plate made from SA508 Grade 4N low-alloy steel. A thermal-metallurgical-mechanical model was developed to predict the temperature, micro-constituents, hardness, distortion and stresses in the EB weldment; the predictions are in good agreement with experimental results. Different restraint conditions on the weld plane were modelled to examine their effects on distortion and stresses. If welding is performed with no restraint, inter-part gapping develops ahead of the beam position that could exceed the tolerance for a sound weld. In contrast, tack welds at the plate ends significantly reduce this gapping, but induce additional tensile stress at the stop-end tack weld. This stress is particularly high as the beam approaches the tack weld. Increasing the extent of the tack weld reduces the tensile stress, while increasing number of distantly distributed narrow tack welds does not help. A full through-length restraint eliminates the opening gap and minimises the development of tensile stresses ahead of the beam that could potentially break the restraint. The applied restraint on the weld plane has little effect on the final residual stress field, since this field mostly develops during cooling after the EB weld is complete. The weld-induced martensitic transformation suppressed tension or promoted compression in the EB weld and heat affected zone (HAZ). A steep gradient of residual stress exists, with high tensile stress concentrated in a narrow region immediately outside the HAZ.

1. Introduction

Electron beam (EB) welding is an advanced joining technique having many advantages over traditional arc welding processes, and it has been increasingly used in energy, automotive, electronics, aerospace and other key industries [1,2]. This technique can generate power densities up to 10^{12} W/m^2 [1], thereby enabling high-speed joining of thick-section components (with thickness up to 250 mm for steel [1]) using a single autogenous weld pass. This unique feature means that EB welding can substantially improve productivity and reduce distortion of thick-section weldments, such as those found in nuclear power plants [2–4]. However, EB welding still faces a number of challenges regarding the requirements of specific applications.

Primary circuit components such as the reactor pressure vessel are both safety-critical and high-value items in nuclear power plants. They are usually made of low-alloy steels, such as SA508 Grade 3 and Grade

4N. Current designs are manufactured dominantly using multi-pass arc welding processes, although power beam welding has been also evaluated for potential applications in new nuclear manufacturing [5–7]. The use of EB welding in the manufacture of primary circuit components requires a thorough understanding of weldment characteristics.

Low-alloy pressure vessel steels exhibit solid state phase transformation (SSPT) during weld-induced thermal cycles. The SSPT complicates the weld microstructures and introduces metallurgical deformation in the fusion zone (FZ) and heat affected zone (HAZ). Desirable microstructures that determine mechanical properties can be obtained through optimising EB welding process [8,9] and post-weld heat treatment [10]. These methods require understanding of the relations between thermal cycles, SSPT, microstructures and mechanical properties. Obasi et al. [11] investigated the complex SSPT behaviour of SA508 Grade 3 steel during weld-like thermal cycles using dilatometry testing and a model for SSPT, and confirmed that both prior-austenite grain size (PAGS) and

Table 1
Chemical composition (in wt.%) of SA508 Grade 4N steel.

C	Si	Mn	Ni	Cr	Mo	V	Al	Cu	Ti	P	Fe
0.067	0.33	0.25	3.31	1.61	0.49	0.01	0.002	0.078	0.001	0.018	Bal.

cooling rate affected the dilatation evolution and final microstructures. Yang et al. [12] demonstrated the effects of quenched microstructures on the impact toughness and temper embrittlement of SA508 Grade 4N steel. They found that the differences in fine blocks, high angle grain boundaries and sulphur segregation determine the effects. Further insights need to be gained for EB weldments, which involve heterogeneous temperatures and cooling rates due to the intense local heating induced by the EB [13,14].

It is well known that EB welding generates little distortion [1,2]. The root cause of this benefit is the extremely localised heat input realised by the highly penetrating EB. However, the focused power beam implies tight tolerance of the gap between opposing faces that are to be joined (a gap above 0.1 mm may not be tolerated for EB welding [1]). This tight tolerance not only requires flat surfaces to work on but also sufficient restraint to ensure that no dangerous opening gap is generated ahead of the moving beam during welding. Tack welds on the EB weld centre plane, i.e., central restraints, are convenient to implement and they are commonly used to prevent part separation, but the rationale behind the design of tack welds has been rarely examined, resulting in a black art potentially facing challenges in different engineering scenarios. In particular, the stresses experienced by the tack welds during EB welding are still poorly understood, although the integrity of tack welds is critical to the success of EB welding. Furthermore, it is still unclear about the effects of the tack welds on residual stresses in EB weldments.

Residual stresses are self-equilibrating stresses due to deformation mismatch [15]. They can be either detrimental or beneficial, depending on the ways they interact with applied load [16–18] and the roles that they play in material degradation [19,20]. Determination of residual stresses is important for assessment of the integrity of welded structures [21]. Recent experimental measurements show that the distributions of residual stresses in EB weldments made of SA508 Grade 3 steel are distinct, compared to arc and laser weldments [22–24]. Weld modelling has proven valuable for understanding residual stresses in SA508 Grade 3 steel EB weldments [25]. Modelling is also necessary to rationalise and inform the design of EB welding process which currently largely relies on experimental trial-and-error. As the SSPT can significantly affect the material properties and residual stresses in weldments [25–32], the analysis of EB welding in low-alloy steels subject to SSPT entails a multiphysics modelling approach.

This study is aimed to investigate the distortion and stress in a SA508 Grade 4N steel EB weld plate, using a thermal-metallurgical-mechanical model validated by experiments. The EB weld model developed here provides comprehensive information about temperature, micro-constituents, hardness, distortion, and in-process stresses and final residual stresses. In particular, different restraint conditions on the weld plane are considered in the weld model, enabling a thorough analysis of the impact of restraint (e.g. tack welds) on EB weld distortion and stresses. This paper is laid out as follows. In Section 2, the material and methods of experiments and modelling are described. In Section 3, the modelling and experimental results are presented. Section 4 is devoted to discussion about the distortion and stresses in the EB weldment. Concluding remarks are made in Section 5.

2. Material and methods

2.1. EB welding in SA508 Grade 4N steel plate

SA508 Grade 4N steel, a candidate material for pressure vessels of advanced reactors, was used for preparation of EB welded plates. The chemical composition of the SA508 Grade 4N steel is shown in Table 1. EB welding was performed to manufacture the SA508 Grade 4N steel plates with dimensions of $300 \times 170 \times 30$ mm, using a Pro-beam® K25 EB facility located at the Nuclear Advanced Manufacturing Research Centre, UK. The EB welding parameters are listed in Table 2. Four nominally identical plates were welded using identical EB welding parameters, so as to facilitate experimental characterisation by different means. All the prepared plates were instrumented with K-type thermocouples on the surfaces at weld mid-length to record transient temperatures corresponding to steady-state welding conditions.

2.2. Modelling

2.2.1. Overview of EB weld model

A 3D sequentially coupled thermal-metallurgical-mechanical model was developed to simulate EB welding of the SA508 Grade 4N steel plate. Fig. 1 shows the dimensions and the finite element (FE) mesh of the weld model developed using the general purpose FE software Abaqus, as well as the thermocouple locations for the four nominally identical plates welded in the experiment. It should be mentioned that the measured distances from the thermocouples to weld centre plane are slightly different between the four plates. A half plate was modelled due to symmetry. Gravity and molten metal flow were not considered in the model, while the weld molten pool was simplified as an arbitrarily defined soft material, a common practice in weld modelling [33]. It was assumed that in the model the EB penetrated through the plate from top to bottom (Fig. 1). The FE model consisted of 28,256 quadratic heat transfer brick elements (Abaqus designation DC3D20) and 28,256 linear reduced-integration brick elements (Abaqus designation C3D8R), for the thermal-metallurgical and mechanical analyses, respectively. The coordinates of the elements were the same between the thermal-metallurgical and mechanical models. The use of linear elements in the mechanical model dramatically reduced the computational time and meanwhile provided satisfactory numerical precision for 3D mechanical analysis [34].

All material properties required for thermal analysis were obtained from ASME 2017, Section II (Materials), Part D (Properties), while the metallurgical properties were obtained through dilatometry tests on the SA508 Grade 4N steel (Section 2.2.3). The temperature-dependent mechanical properties of the SA508 Grade 4N steel were derived from previous tensile test data supplied by Wood plc (Section 2.2.4). For the coordinate system used, the X (1), Y (2) and Z (3) directions correspond to the transverse, normal and longitudinal directions of the plate, respectively, as shown in Fig. 1. It should be mentioned that in following sections the stress unit is MPa and the weld refers to the EB weld, unless otherwise stated.

2.2.2. Thermal model

A bespoke weld modelling tool, FEAT-WMT [36], was used to calibrate the idealised heat source for the thermal model. A double-ellipsoidal conical idealisation of the input power distribution was adopted (Fig. 1). This has proven effective to capture the heat flux associated with the keyhole mode of EB welding [35]. The volumetric power density is defined as:

$$q = \begin{cases} q_{fe} & \text{if } y - y_c < 0, z > z_c \\ q_{re} & \text{if } y - y_c < 0, z \leq z_c \\ q_{fc} & \text{if } 0 \leq y - y_c < h_c, z > z_c \\ q_{rc} & \text{if } 0 \leq y - y_c < h_c, z \leq z_c \end{cases} \tag{1}$$

Table 2
Parameters of EB welding in horizontal position (2G position).

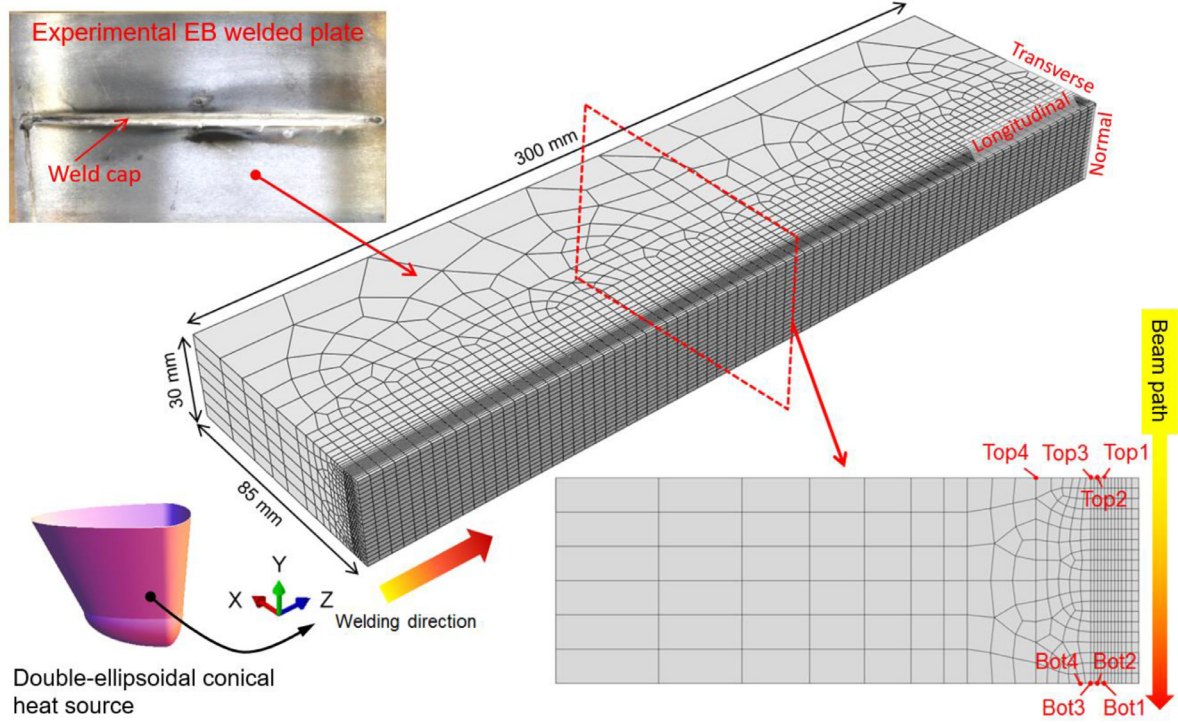| Voltage (kV)	Current (mA)	Speed (mm/s)	Circular figure amplitude (mm)	Frequency (Hz)
80	350	8.3	X: 2; Y: 2	222

Fig. 1. Geometry and mesh of FE model for EB welding. Only half plate is considered due to symmetry. The upper left inset shows the photograph of a welded plate and the lower left inset shows the schematic of double-ellipsoidal conical heat source [35]. The lower right inset shows the details of the FE mesh on the mid-length section and the thermocouple locations. Note that in the model the EB is assumed to penetrate the plate from the top to bottom.

where

$$q_{\text{fe}} = \frac{Q}{N_{\text{int}}} \frac{12\sqrt{3}R_{\text{fe}}}{ac_{\text{f}}b\pi\sqrt{\pi}} \exp\left(-3\left(\frac{(x-x_c)^2}{a^2} + \frac{(y-y_c)^2}{b^2} + \frac{(z-z_c)^2}{c_{\text{f}}^2}\right)\right) \quad (2)$$

$$q_{\text{re}} = \frac{Q}{N_{\text{int}}} \frac{12\sqrt{3}R_{\text{re}}}{ac_{\text{r}}b\pi\sqrt{\pi}} \exp\left(-3\left(\frac{(x-x_c)^2}{a^2} + \frac{(y-y_c)^2}{b^2} + \frac{(z-z_c)^2}{c_{\text{r}}^2}\right)\right) \quad (3)$$

$$q_{\text{fc}} = \frac{Q}{N_{\text{int}}} \frac{108e^3 R_{\text{fc}}}{(e^3-1)aD_{\text{f}}h_c\pi^2} \exp\left(-3\left(\frac{(x-x_c)^2}{\Gamma_{\text{a}}^2} + \frac{(z-z_c)^2}{\Gamma_{\text{fc}}^2}\right)\right) \quad (4)$$

$$q_{\text{rc}} = \frac{Q}{N_{\text{int}}} \frac{108e^3 R_{\text{rc}}}{(e^3-1)aD_{\text{r}}h_c\pi^2} \exp\left(-3\left(\frac{(x-x_c)^2}{\Gamma_{\text{a}}^2} + \frac{(z-z_c)^2}{\Gamma_{\text{rc}}^2}\right)\right) \quad (5)$$

In the above equations, q is the power per unit volume and Q is the total power input; e is Euler's number; (x_c, y_c, z_c) indicates the centre of the double ellipsoidal heat source; a and b are the lateral and vertical radii, respectively; c_{f} and c_{r} are the axial radii ahead of and behind the beam, respectively; h_c is the height of the conical source; $\Gamma_{\text{a}} = a - (a - a_{\text{i}})(y - y_c)/h_c$, $\Gamma_{\text{fc}} = c_{\text{f}} - (c_{\text{f}} - c_{\text{fi}})(y - y_c)/h_c$ and $\Gamma_{\text{rc}} = c_{\text{r}} - (c_{\text{r}} - c_{\text{ri}})(y - y_c)/h_c$ where a_{i}, c_{fi} and c_{ri} are user defined parameters; the R_{fe}, R_{re}, R_{fc}, R_{rc}, D_{f} and D_{r} are all functions of a, b, c_{f}, c_{r}, a_{i}, c_{fi} and c_{ri}, see detailed expressions in Ref. [35]; and N_{int} is an integral over the total volume of material, as used to ensure that the total power input is equal to Q.

The idealised heat source was calibrated using FEAT-WMT and then imported into the Abaqus thermal model to predict the temperature field in the plate. User-defined Abaqus subroutines UEXTERNALDB and DFLUX were employed for thermal analysis. Only radiation heat loss

was considered during welding, as it was performed in a vacuum chamber, while both radiation and convection heat loss was considered when the welded plate was exposed to air for cooling to room temperature. The predicted transient temperature field was used for subsequent metallurgical analysis.

2.2.3. Metallurgical model

In the EB weld model, SSPT and austenite grain growth were modelled using a semi-empirical approach implemented in Abaqus subroutine UVARM, which has been elaborated in Refs. [26,37]. It should be noted that chemical dilution and in-process tempering [38–40] is irrelevant here, since EB welding is a single-pass autogenous process. For brevity, only key information is provided here and more details can be referred to Refs. [26,37].

In the HAZ, austenitisation kinetics is captured using the Leblond-Devaux model [41], viz.

$$\dot{x} = \frac{x_{\text{eq}} - x}{\tau_{\text{LD}}} \quad (6)$$

where x_{eq} and τ_{LD} are temperature-dependent parameters, indicating an equilibrium fraction of austenite and an empirical retardation factor [42], respectively. Table 3 shows the parameters adopted in the model. The characteristic temperatures of 760 °C and 815 °C were obtained from dilatometry tests, as described later. In the FZ, 100% austenite is presumed to form as soon as the temperature drops below the melting point.

The austenite grain growth kinetics incorporated in the EB weld model is only capable of capturing the growth of equiaxed austenite in the HAZ. The size of austenite grains in the FZ was approximated to

Table 3
Parameters used in the austenitisation kinetics model.

Temperature (°C)	x_{eq}	τ_{LD} (s)
<760	0	1
760	0	1
815	1	0.2
>815	1	0.05

Note: Linear interpolation is used between 760 °C and 815 °C.

be 50 μm. In general, grain growth can be modelled using the equation below [43]

$$\frac{dL}{dt} = C \exp\left(-\frac{Q}{RT}\right)\left(\frac{1}{L} - \frac{1}{L_{lim}}\right) \tag{7}$$

where L is austenite grain size, L_{lim} is the maximum grain size attainable at a temperature below a grain coarsening temperature T_c [43], Q is the activation energy of grain growth, R is the universal gas constant, T is absolute temperature and C is a material constant. When the temperature exceeds T_c (taken to be 1020 °C [38]), the term $1/L_{lim}$ vanishes. The values of the parameters in Eq. (7) were all taken from Ref. [38].

Austenite decomposition upon cooling is captured using a reaction kinetics model originally proposed by Kirkaldy and Venugopalan [44] and later refined by Li et al. [37]. In this SSPT model, the time required to form a fraction X of an isothermal transformation product (e.g. ferrite, pearlite and bainite) at a temperature T (in K) is expressed as

$$\tau(X, T) = \frac{F(C, Mn, Si, Ni, Cr, Mo, G)}{\Delta T^n \exp(-Q/RT)} S(X) \tag{8}$$

where F is a function of chemical composition (i.e. weight percentages of C, Mn, Si, Ni, Cr and Mo) and ASTM grain size number (G), and F differs between ferrite, pearlite and bainite transformations; $S(X)$ is a function exhibiting a sigmoidal shape; ΔT is undercooling; Q is activation energy; R is the universal gas constant; and n is an empirical exponent. The specific forms of F and S, and the values of all the parameters in Eq. (8), can be found in Refs. [26,37]. The Ae_3, Ae_1 and B_s temperatures, which indicate the start of the transformations of ferrite, pearlite and bainite, are estimated using empirical equations in terms of chemical composition [26,37]. The anisothermal transformation kinetics were captured using an additivity rule [26] based on the isothermal kinetics model shown in Eq. (8).

The modelling of martensitic transformation employs the Koistinen-Marburger equation [45] and the martensite fraction is given by

$$X = X_{RA}\{1 - \exp\left[-A(M_s - T)\right]\} \tag{9}$$

where X_{RA} is the fraction of austenite available for martensitic transformation, M_s is the martensite start temperature and A is a material parameter (A = 0.035 K^{-1} for SA508 steel [46]). M_s is estimated based on the chemical composition [26,37].

To verify the efficacy and accuracy of the SSPT model, free dilatometry tests were conducted on the SA508 Grade 4N steel. Two peak temperatures, i.e. 900 °C and 1200 °C, were chosen to represent fine-grained HAZ (FGHAZ) and coarse-grained HAZ (CGHAZ) samples, respectively. The measurement method and experimental procedures were the same as detailed in Ref. [11]. Fig. 2a compares the predicted and measured continuous cooling transformation (CCT) start temperatures. The overall agreement is good, although some details differ. In particular, the model predicted mixed micro-constituents at cooling rates lower than 20 °C/s, while multiple phases, if any, could not be conclusively distinguished from the dilatometry data. Fig. 2b and 2c shows the predicted and measured dilatation curves at cooling rates typical for a welding process [38,40]. The agreement is good in terms of the overall trend, despite a discrepancy in strain at the final state. Marked residual compressive strains were observed in the measurements, which could be attributed

to retained austenite and/or micro-plasticity. Although retained austenite up to 6% has been identified in as-quenched Grade 4N steel [47], its fraction is too low to cause such an amount of residual strain. Since the dilatometry samples were free from mechanical loading except a negligible force for sample holding, the potential micro-plasticity is unlikely to be driven by external load but might arise from transformation plasticity driven by back stress, which is dependent on material history [48]. By contrast, the model did not predict any retained austenite or plastic deformation (no transformation plasticity was predicted, as no external load was applied and no back stress was considered in the model). Nevertheless, the agreement between the predictions and measurements is deemed overall satisfactory, confirming the efficacy and accuracy of the SSPT model adopted for the EB welding in the SA508 Grade 4N steel.

2.2.4. Mechanical model

In the mechanical model, three different restraint conditions were applied on the weld centre plane to take account of symmetry and to prevent rigid body motion of the weldment. These are referred to as full restraint, no restraint and tack-weld restraint, as shown in Fig. 3. In the first case, i.e., full restraint (Fig. 3a), out-of-plane displacement was directly set to be zero over the entire symmetry plane. This assumption treats the two half-plates in the real weldment as a single monolithic plate. In the second case, i.e., no restraint (Fig. 3b), the two half-plates were allowed to separate, but not to interpenetrate, on the symmetry plane, using the cohesive elements described in next paragraph. For tack-weld restraint, two regions (4 × 30 mm for each) at the two ends of the plate were restrained from out-of-plane displacement, as shown in Fig. 3c, mimicking the two tack welds in the real welding experiment (Fig. 3d), while the rest of the weld centre plane was allowed to separate, but not to interpenetrate. The mechanical properties of the tack weld were presumed to be the same as those of the base material. The tack welding process was not modelled, so no residual stresses, distortions or microstructural changes were associated with the tack welds.

Cohesive elements (Abaqus designation COH3D8) were used to capture the restraint conditions shown in Fig. 3b and 3c. An additional thin layer (0.1 mm thick) of cohesive elements was added, with one side attached to the weld centre plane and the other side fixed. Out-of-plane motion of the weld centre plane nodes was controlled via changing the out-of-plane stiffness of the cohesive elements, while the in-plane stiffness of the cohesive elements was assumed low enough to allow in-plane nodal motion throughout the EB welding. In the restrained condition, the out-of-plane stiffness was set high enough to prevent motion in either out-of-plane direction. In the unrestrained condition, separation (gapping) of the two plate halves was allowed by assigning a low stiffness for motion in this direction, while interpenetration was prevented by retaining a high stiffness for motion in the opposite direction. Between the restrained and unrestrained regions, a transition in stiffness exists within one cohesive element (approximately 4 mm long). To simulate the progressive establishment of restraint behind the electron beam, restraint was imposed on the weld centre plane immediately after the heat source had passed the relevant cohesive elements. It should be mentioned that the rise in the out-of-plane stiffness of cohesive elements occurs at high temperature as the heat source passed the element. The rise in the out-of-plane stiffness can cause a drastic reduction in elastic deformation of the cohesive elements, which had undergone separation before the heat source passed. This can be accommodated by the plastic deformation of the molten material which is set to be very soft at high temperature.

Plastic deformation of the SA508 Grade 4N steel and its transformation products was modelled using a Lemaitre-Chaboche hardening model. This model incorporates both the Bauschinger effect, where the yield strength in a given loading direction is reduced by prior plastic flow in the opposite direction, and cyclic hardening. Both these phenomena are important in welding, where the thermomechanical loading is cyclic, with compressive plastic flow in the heating phase and tensile plastic flow during the cooling phase. Previous studies show that
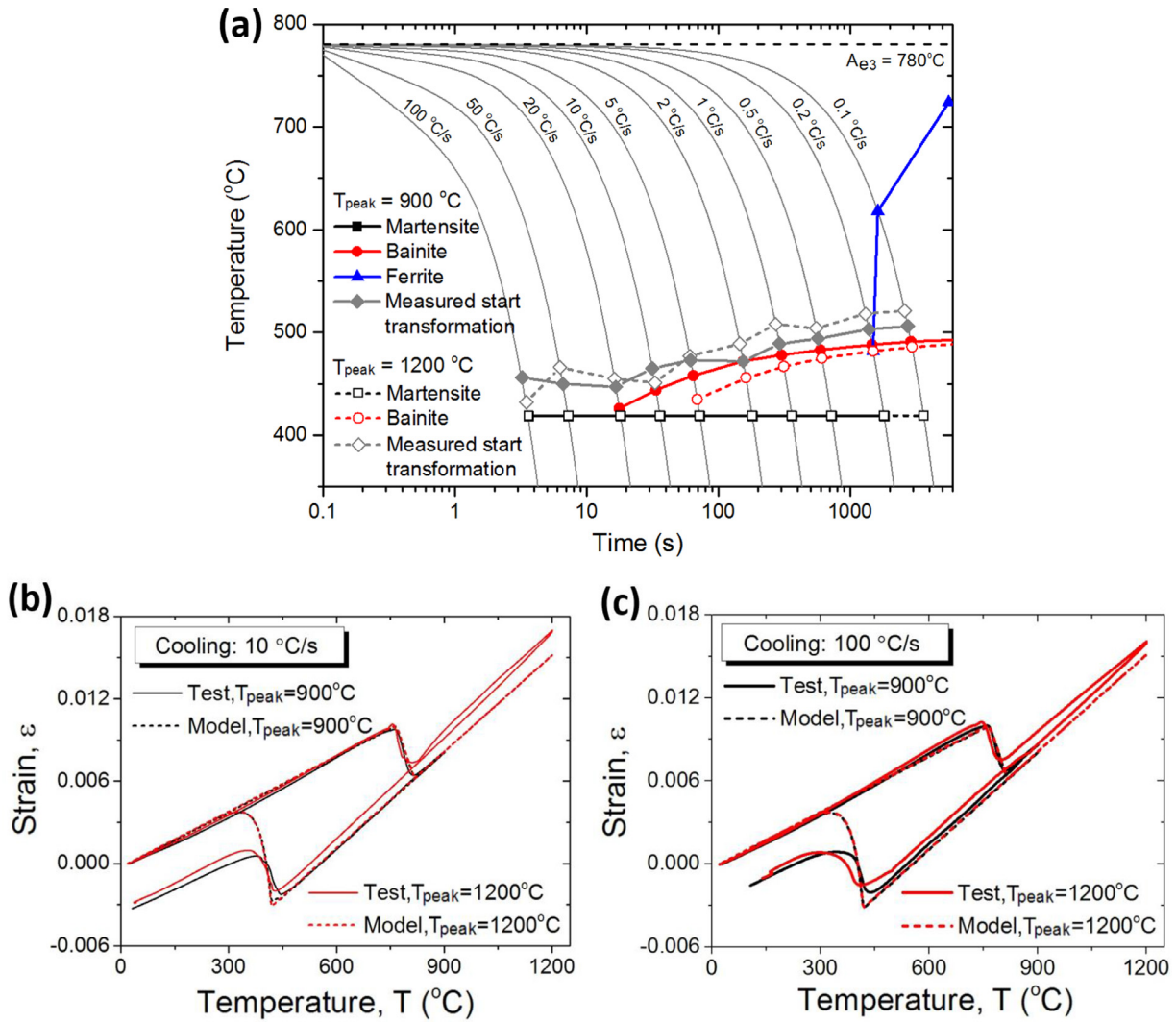
Fig. 2. Comparison of measured and predicted metallurgical properties of SA508 Grade 4N steel: (a) continuous cooling transformation diagram (A_{e3} temperature in the plot was determined using Thermo-Calc software); (b) dilatation curves at a cooling rate of 10 °C/s; (c) dilatation curves at a cooling rate of 100 °C/s. Note that prior austenite grain sizes of 11 μm and 65 μm [11] were used in the SSPT model for peak temperatures of 900 °C and 1200 °C, respectively.

the magnitude of cyclic isotropic hardening in SA508 steel is normally insignificant [50], so only the Bauschinger effect need be considered, particularly in a single pass weld. This study follows Ref. [26] in employing non-linear kinematic hardening. In the Lemaitre-Chaboche model, multiple kinematic hardening components or back stresses can be superposed. It was found that the use of a single back stress was sufficient to accurately fit the available tensile stress-strain test data [51]. Hence, the following kinematic hardening equation was used

$$\dot{\alpha} = C \frac{1}{\sigma^0} (\sigma - \alpha) \dot{\bar{\varepsilon}}^{pl} - \gamma \alpha \dot{\bar{\varepsilon}}^{pl} \qquad (10)$$

where $\dot{\alpha}$ is the back stress rate, $\dot{\bar{\varepsilon}}^{pl}$ is the equivalent plastic strain rate, σ^0 is the size of the yield surface, and C and γ are material parameters. Lemaitre-Chaboche model parameters may be fitted to data from either monotonic tensile tests or isothermal cyclic tests (for example, see Refs. [52,53]). In this case, only monotonic test data were available. Table 4 shows the plasticity parameters derived from these data. It should be noted that, for the transformation products (e.g. austenite, martensite and bainite), the parameter σ^0 was scaled according to the hardness ratios between the SA508 Grade 4N steel and its transformation products, while other hardening parameters were kept the same. The plastic properties of different micro-constituents are controlled by field vari-

ables which are updated in Abaqus subroutine USDFLD, in accordance with the SSPT model.

The thermal expansion coefficients for individual ferritic and austenitic phases were derived from the dilatometry tests (Fig. 2b and 2c) through linear fitting of the heating and cooling portions of the measured dilatation curves, respectively, which are 13.7×10^{-6}/°C and 23.6×10^{-6}/°C for the ferritic and austenitic phases, respectively. The thermal-metallurgical volumetric deformation due to weld-induced thermal cycles was determined using a rule-of-mixtures based on the decoupled dilatation curves (Fig. 2b and 2c), and the numerical algorithm [26] was implemented in Abaqus subroutine UEXPAN. Transformation-induced plasticity (TIP) was also considered, following Leblond et al. [54], viz.

$$\dot{\varepsilon}_{ij}^{tp} = \frac{3}{2} K s_{ij} f'(z) \dot{z} \qquad (11)$$

where $\dot{z}$ is the rate of phase transformation, $f(z)$ is a normalised function, s_{ij} is the deviatoric stress, and K is a material constant. For SA508 steel, we have $f(z) = z(2 - z)$ and $K = 10^{-4}$ MPa^{-1} [54].
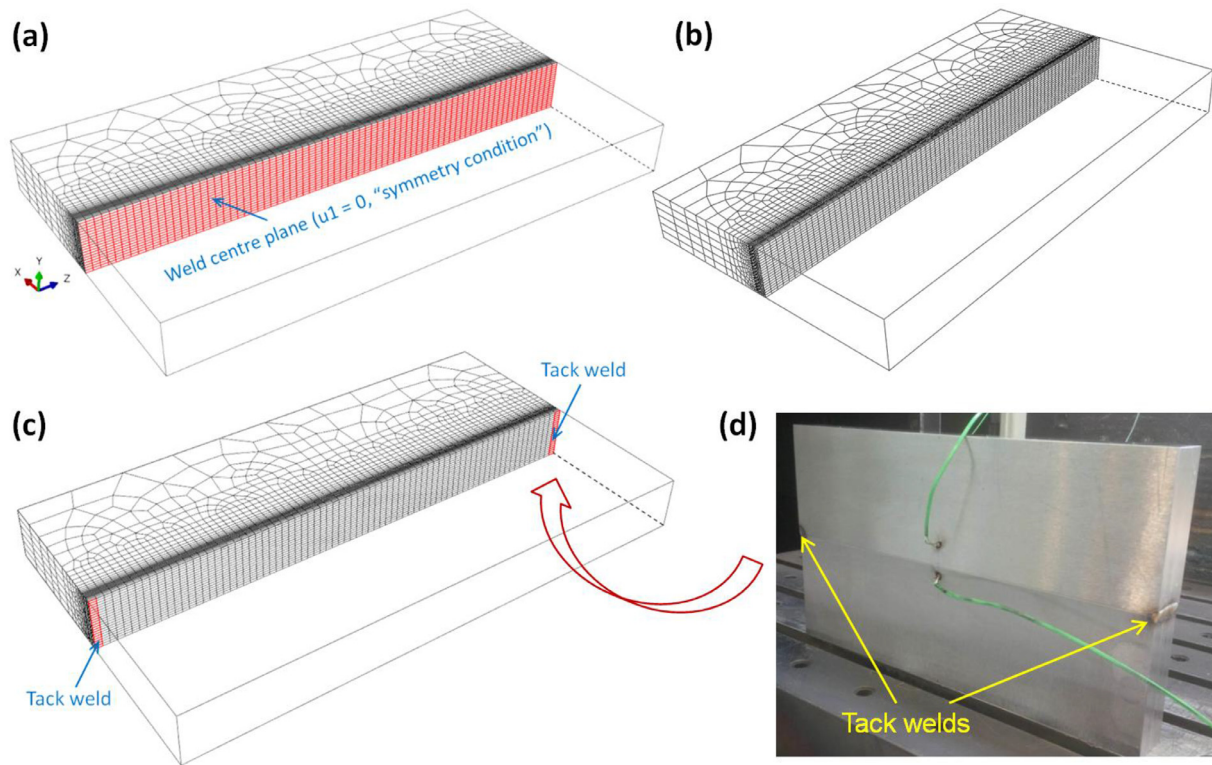
Fig. 3. Illustration of the boundary condition on the EB weld centre plane: (a) traditional symmetry condition, i.e. no out-of-plane displacement (full restraint); (b) out-of-plane displacement is allowed only for separation before heat source passes (this is denoted as no restraint), but not allowed afterwards; (c) is identical to (b) except the tack weld location where out-of-plane displacement is not allowed, i.e. partial restraint. (d) shows the experimental configuration of two identical steel parts that were tack-welded at the two ends of the plate before EB welding [49].

Table 4
Fitting parameters in Lemaitre-Chaboche model for SA508 Grade 4N steel.

	Temperature (°C)							
	21	100	200	300	400	500	600	700
σ^0(MPa)	754	711	669	658	612	524	412	162
C(MPa)	3902	3600	3720	3820	5614	11492	259	4600
γ	15.03	15.03	15.03	15.03	39.02	305.81	305.81	305.81

2.3. Characterisation and measurements

A 5-mm thick transverse slice was extracted from the mid-length section of the welded plate and used for microscopic characterisation and hardness measurement. The sample for scanning electron microscope (SEM) characterisation was prepared following standard grinding and polishing methods and etched in 2% Nital. An FEI Quanta 650 SEM operating at an accelerating voltage of 20 kV and in a secondary-electron imaging mode was used to capture micrographs of FZ, CGHAZ and FG-HAZ. Hardness measurements were performed on the mid-length slice using a Durascan™ tester. A matrix of 2193 points was used with spatial resolution of ~ 0.4 × 0.4 mm and a load of 0.3 kgf, producing maps which spanned the FZ, HAZ and base material at either side of the weld.

Weld residual stresses were measured on the KOWARI neutron beamline at the Australian Nuclear Science and Technology Organisation (ANSTO). The measurements using {211} reflection were performed in the mid-length plane and employed a gauge volume of 3 × 3 × 3 mm for the longitudinal stress and of 3 × 3 × 10 mm for the normal and transverse stresses. The choice of 10 mm in the longitudinal direction for some of the measurements was made to reduce measurement time, which can be justified by the approximately uniform distribution of stresses along the longitudinal direction when the measurement locations are far from the plate ends.

3. Results

3.1. Temperature

Fig. 4 compares the predictions and measurements of temperature evolution at the thermocouple locations (Fig. 1) on the plate surfaces. It is evident that both the peak and transient profiles of the temperature histories have been captured by the weld model. Fig. 5a and 5b show the observed metallurgical boundaries (i.e. FZ and HAZ boundaries) and predicted isothermal lines with regard to peak temperature, respectively. The critical temperatures for melting and austenitisation of the SA508 Grade 4N steel are 1450 °C and 760 °C, respectively, which were estimated by thermodynamic analysis using Thermo-Calc software and measured through dilatometry tests, respectively. The predicted isothermal lines for melting and austenitisation are consistent with the observed FZ and HAZ boundaries in the macrograph (Fig. 5a), respectively.

Since both the predicted evolution (Fig. 4) and distribution (Fig. 5a, b) of temperature agree well with experimental results, it can be concluded that the idealised heat source and the thermal solution of the weld model are sufficiently accurate for analyses of SSPT, stress and distortion which are mainly determined by material behaviour in solid state, and such a verification of thermal model accuracy has been recom-
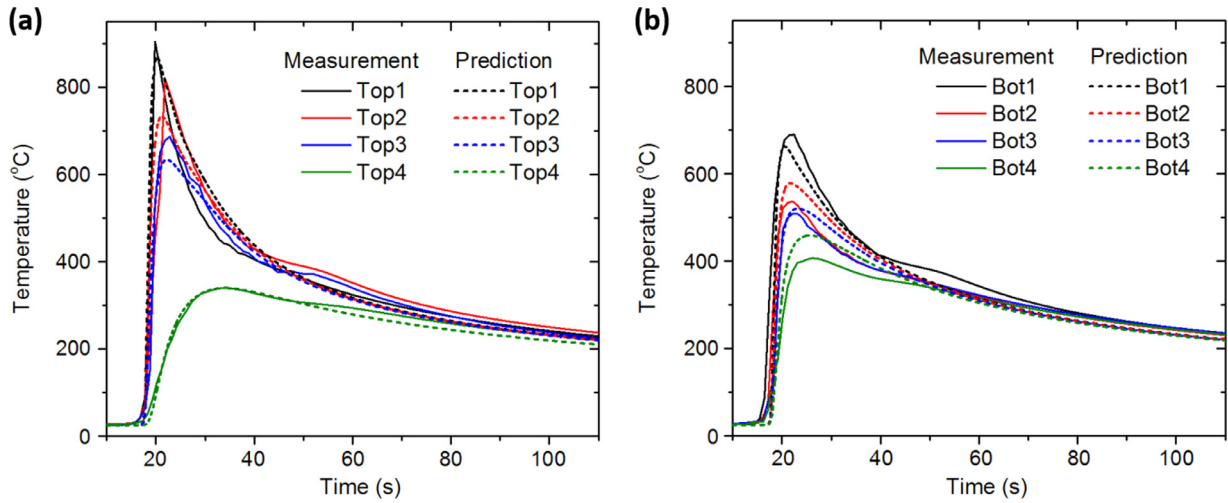
Fig. 4. Comparison between predicted and measured temperature histories at the thermocouple locations (see Fig. 1) on top surface (a) and bottom surface (b) of the EB weld plate.
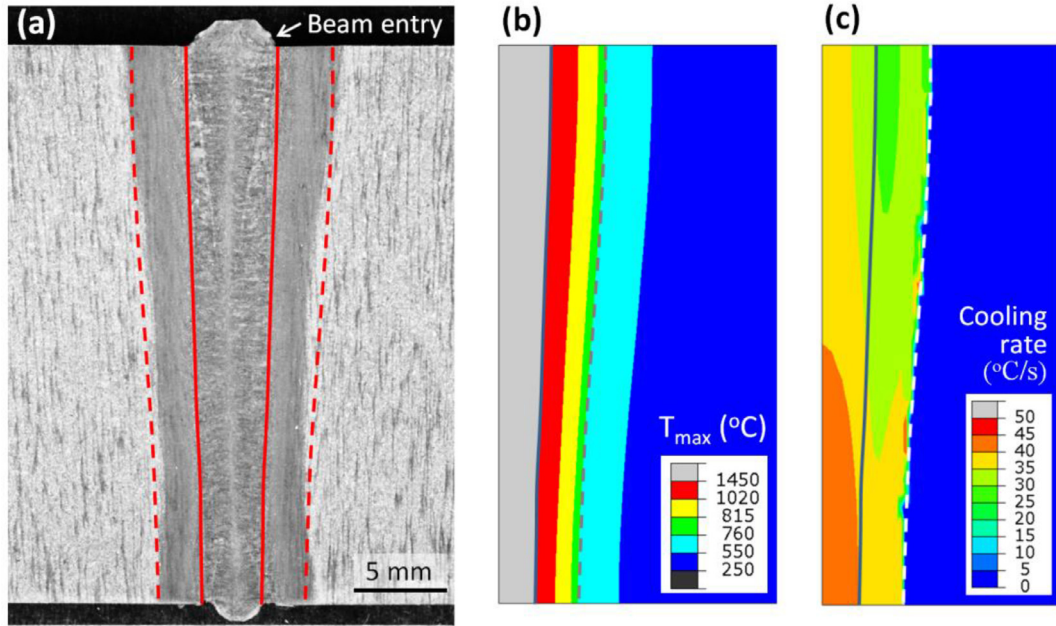

Fig. 5. (a) Mid-length macrograph of the EB weld; (b) predicted distribution of peak temperature; (c) predicted distribution of cooling rate at 700 °C. Note that the predicted isothermal lines that correspond to the FZ boundary (solid line) and HAZ boundary (dashed line) are superposed in the macrograph shown in (a).

mended by R6 structural integrity assessment procedure [55,56]. However, for analyses of solidification process and structure, more accurate thermal models such as those based on computational fluid dynamics are needed to realistically capture the temperature field in the weld pool. Fig. 5c shows the predicted cooling rates at 700 °C. In the FZ and HAZ, the cooling rates fall in the range of 20–50°C/s. As expected, the cooling rate drops with increasing distance from the weld centreline. In addition, it is also evident that the weld root cools faster than the weld crown. Such a difference in cooling rate may have significant implications in the development of microstructures, as shown in Fig. 2a.

3.2. Microstructure and hardness

Fig. 6 shows the observed and predicted microstructures. Prior austenite grain boundaries are clearly seen in the SEM images, showing columnar and equiaxed grains in the FZ (Fig. 6a) and HAZ (Fig. 6b

and 6c), respectively. The linear-intercept PAGS estimated from a series of micrographs falls in the range of 10–90 μm, similar to the range of 3–70 μm predicted by the weld model. The SEM images show that a microstructure with fine laths is dominant in the FZ and HAZ (Fig. 6a-c). The predicted fractions of martensite and bainite (Fig. 6d) in the FZ and HAZ are consistent with these microscopic observations (Fig. 6a-c). It should be mentioned that the untransformed base material (blue region outside HAZ, as shown in Fig. 6d) was not characterised here and treated as a predefined independent phase in the SSPT model.

As microstructure determines mechanical properties, an empirical correlation between different micro-constituents and hardness has been established [57]. In the weld model developed here, a rule-of-mixtures is used to estimate the Vickers hardness based on the predicted fractions of micro-constituents and their individual hardness [26,37]. Fig. 7 compares the predicted and measured hardness distributions on the mid-length section of the EB welded plate. From the hardness contour
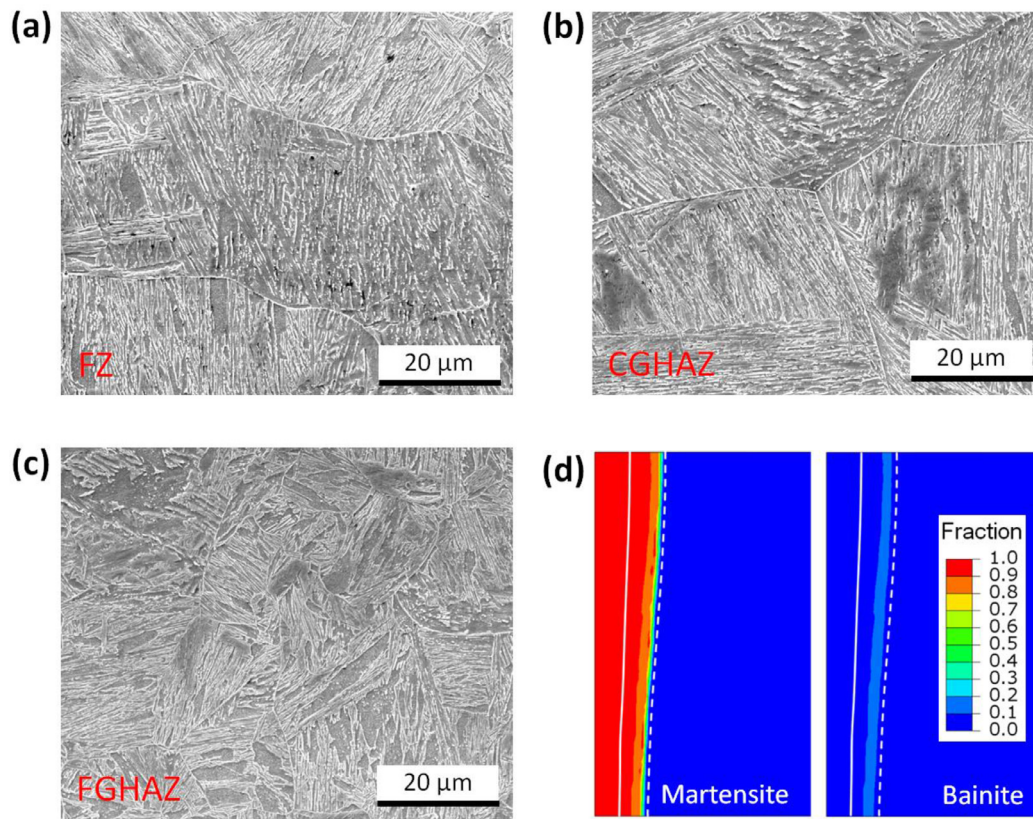
Fig. 6. SEM images for microstructures in FZ (a), CGHAZ (b) and FGHAZ (c). The predicted distributions of martensite and bainite are shown in (d), wherein the solid and dashed lines indicate the predicted FZ and HAZ boundaries, respectively.

maps, an overall good agreement between prediction and measurement is clearly seen. The line profiles of measured hardness distributions in the top, middle and bottom show that the hardness increases rapidly across the HAZ boundary and then reaches a plateau (~360 HV) with some fluctuation in the HAZ and FZ. The weld model correctly predicted the hardness, despite relative smoothness in predicted distribution compared to somewhat scatter in measurement data. The agreement between the prediction and measurement results of hardness verifies the good accuracy of the metallurgical prediction for microstructure. Microhardness values of 350 HV and above are expected to arise from a predominantly martensitic structure, which is consistent with the results shown in Fig. 6. The heterogeneous hardness distribution also indicates that the yield strengths of the FZ and HAZ are significantly higher than that of the base material.

3.3. Distortion

Fig. 8 shows the transverse displacement distributions on the top surface of the plate at different stages of EB welding. When the weld centre plane is not restrained, an opening gap is generated and its half width (only half plate is modelled) reaches 0.8 mm when the heat source just passes mid-length of the plate (Fig. 8a). The use of tack welds on the two ends of the plate effectively reduces the transverse expansion during the welding, despite a small gap generated immediately ahead of the heat source at the beginning of the welding, as shown in Fig. 8b. For full restraint on the weld centre plane (see Fig. 3a), no gap is generated throughout the welding process (Fig. 8c). In the final state after cooling to room temperature, it is clearly seen that transverse shrinkage occurs in the welded plate under tack-weld or full restraint, particularly in the mid-length section, as shown in Fig. 8b and 8c. By contrast, the model with no restraint predicts an increasing transverse expansion towards the weld stop in the final state. It should be noted that there is a caveat

on the above results, i.e., the weld model does not take into account the potential loss of material in the weld, due to metal evaporation and molten metal flow under the 2G welding position (Figs. 1 and 3d), which are not uncommon for EB welding [1].

In the no restraint case, the development of gap is further examined via tracking the evolution of transverse displacement of FE nodes on the weld centre plane, as shown in Fig. 9. The largest transverse displacement of 0.95 mm (i.e. a full gap width of 1.9 mm) occurs at the top of the weld stop end, soon after the welding starts, and then the transverse displacement fluctuates about 0.8 mm during the welding and drops to zero when welding completes. The difference in transverse displacement between the top and bottom of the plate is within 0.1 mm, while the transverse displacement at the mid-length location is approximately half that at the weld stop end. The gap that developed at the mid-length location disappears when half weld is completed, due to the establishment of restraint on separation by the EB weld itself.

Fig. 10 shows another detailed comparison of distortion for both top and bottom surfaces on the mid-length section. It is evident that transverse expansion during welding is promoted by no restraint, which also largely reduces the transverse shrinkage and even causes transverse expansion in the final state. The transverse expansion during welding is marginal for both tack-weld restraint and full restraint, for which the transverse shrinkage in the final state is pronounced. In general, tack-weld restraint causes slightly more expansion and less shrinkage than full restraint. Within a distance of 10 mm from the weld centre, the transverse displacement quickly increases and then approximates constant towards the lateral side of the plate, indicating the concentration of deformation around the weld. The transverse displacement distributions on the top and bottom surfaces are similar, despite some difference in details. The slight difference can be attributed to the wider FZ and HAZ near the top surface, in comparison with the bottom surface (Fig. 5a).
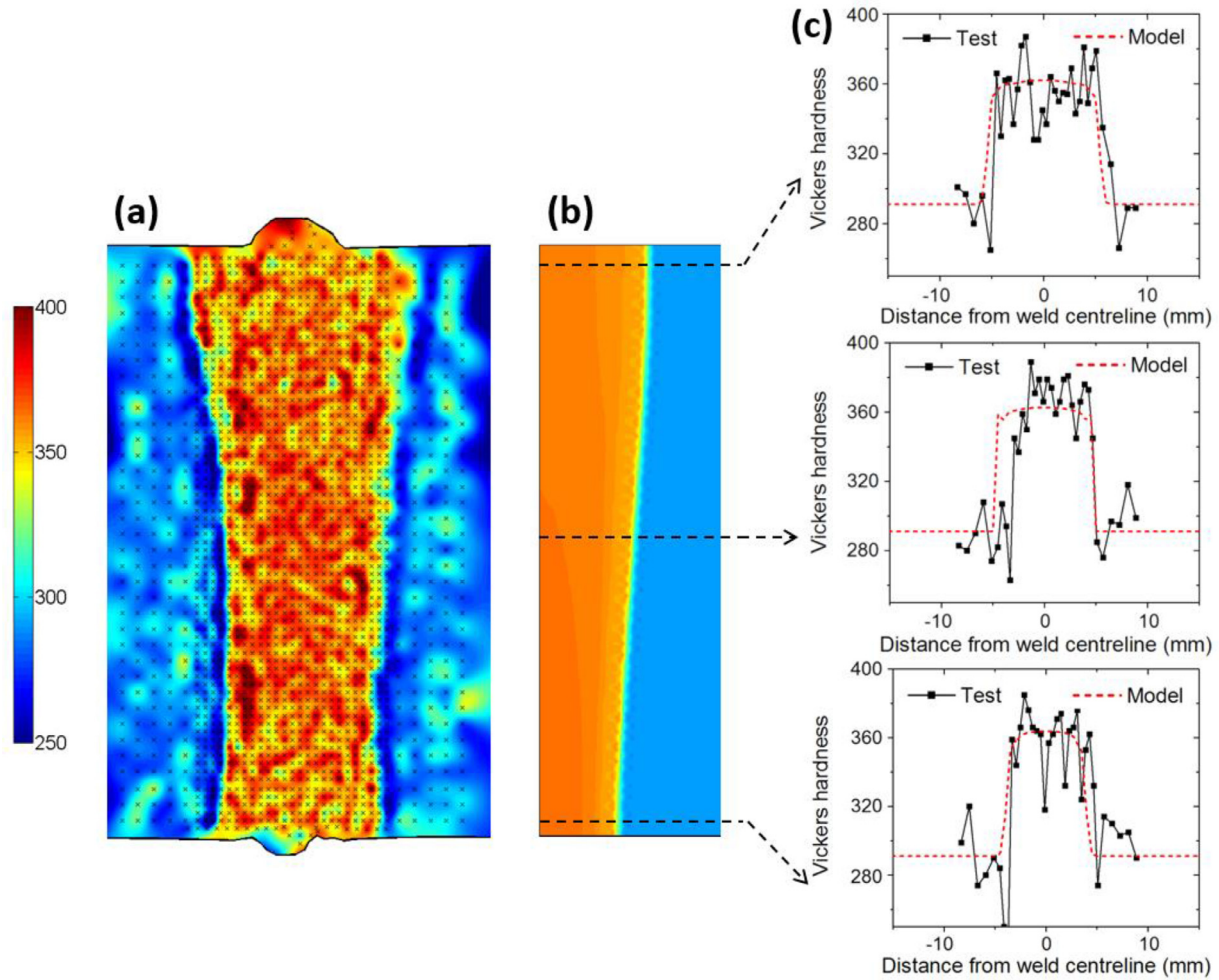
Fig. 7. Contour maps of measured (a) and predicted (b) Vickers hardness distributions on the mid-length section. Line profiles of the hardness distribution in the top, middle and bottom are also shown (modelling results are mirrored about the weld centreline).
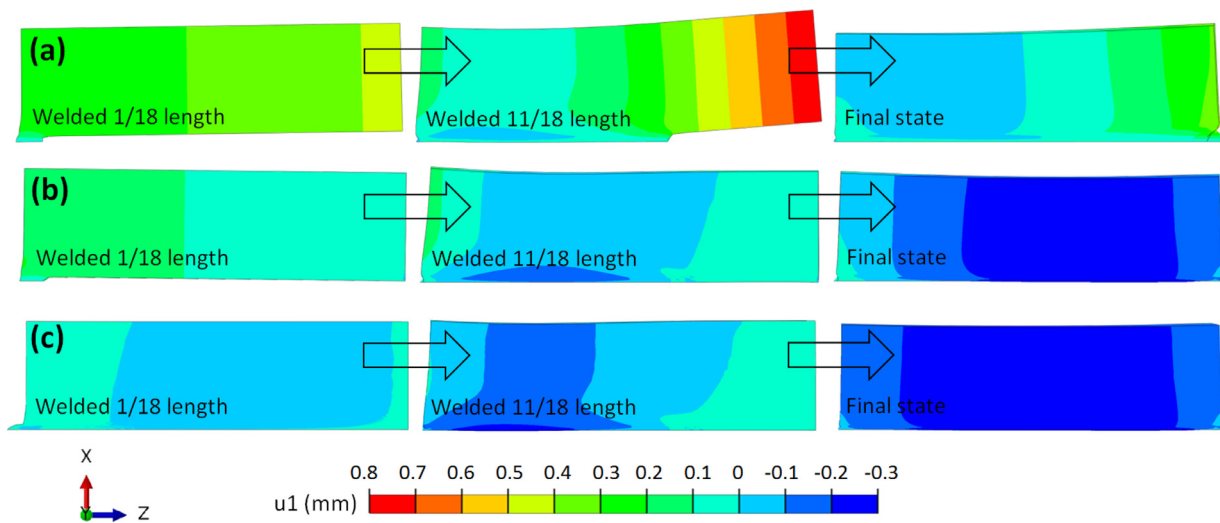

Fig. 8. Predicted transverse displacement distributions on the top surface of the plate in different stages of EB welding when no restraint (a), tack-weld restraint (b) or full restraint (c) was applied. Note that the displacement is scaled by a factor of 20 to facilitate visualisation.
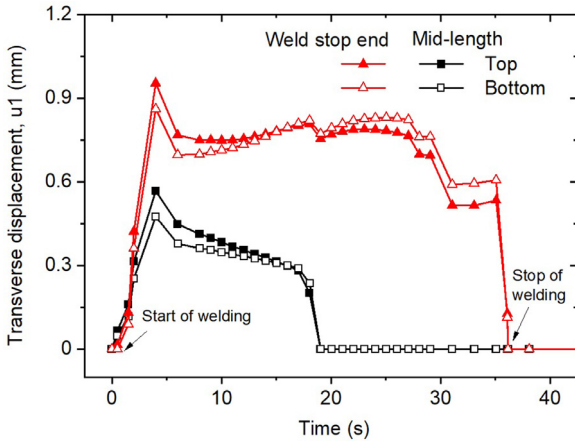
Fig. 9. Evolution of transverse displacement of FE nodes at different positions on weld centre plane during welding in the no restraint case.
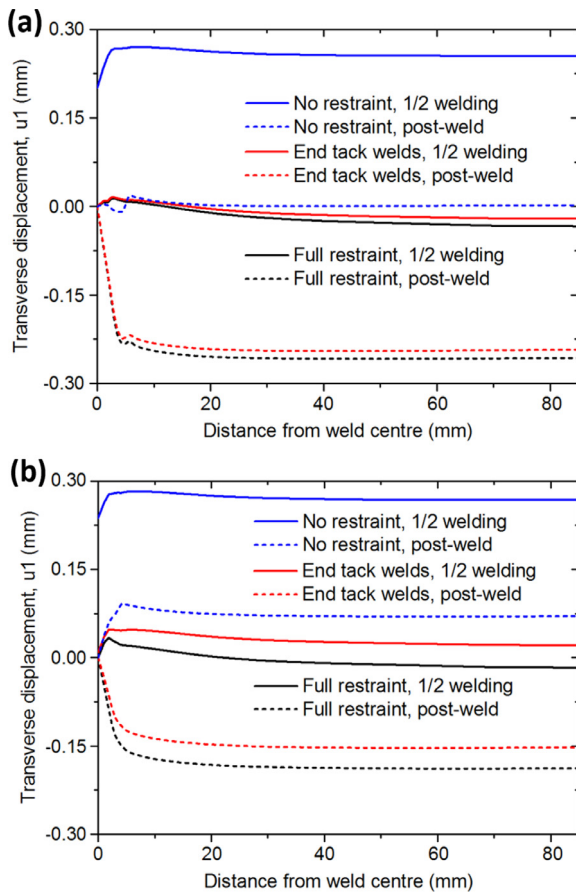
Fig. 10. Line profiles of transverse displacement distribution on mid-length section: (a) top surface; (b) bottom surface.

3.4. Stresses

Fig. 11 shows the 3D distributions of predicted residual stresses in the EB welded plate when full restraint on the weld centre plane was applied. Fig. 11a shows the prediction for longitudinal residual stress. The stress distribution is distinct, showing high compressive stresses, near the weld start and stop ends, between which the stress distribution is approximately uniform through the plate length. Fig. 11b shows the prediction for normal residual stress. Again, the stress is approximately uniformly distributed along the plate length, except at the weld

ends where the stress magnitude is overall lower. For transverse residual stress, as shown in Fig. 11c, peak tensile stress is found at the cap and root of the weld, while peak compressive stress is concentrated outside the weld, at the two ends and near the top and bottom surfaces. Overall, the magnitude of transverse stress is lowest compared to the longitudinal and normal stresses.

The measured and predicted contour maps of longitudinal residual stresses on the mid-length section are shown in Fig. 12a and 12b, respectively. The revealed features of stress distribution are similar between measurement and prediction, i.e., tensile stress with low magnitude (or compressive stress) is generated in the FZ and HAZ, while tensile stress with high magnitude is generated in the base material just outside the HAZ. It is clearly seen that there is a steep change of stress across the HAZ boundary towards the base material.

The magnitude of the predicted stress is overall higher than that of the measured stress. Considering the gauge volume used in the neutron diffraction measurement (Section 2.3), it is necessary to examine the effect of averaging on the determined stress. Fig. 12c shows the predicted stresses averaged over different gauge domains. It is evident that averaging leads to significant reduction in the obtained peak stress, due to the high gradient of stress. Fig. 12d shows the stress distributions in the top, middle and bottom. For consistency, the predicted stresses are averaged over a width of 3 mm (Section 2.3) in the mid-length plane and then are compared with the measurement results. Overall the agreement is good, despite some discrepancy in peak stresses. Difficulty is anticipated for neutron diffraction measurements to capture the peak stresses using the aforementioned gauge volume [58]. In addition, the density of the measurement points (grey cross marks in Fig. 12a) was limited due to the restriction of access time to neutron source, and consequently the measurements might miss the locations of peak stresses.

The distribution of normal stress on the mid-length section (Fig. 13a) is similar to that for the longitudinal stress (Fig. 12b), despite difference in the stress magnitude, i.e., the compressive stress is higher, but the tensile stress is lower for the normal stress than for the longitudinal stress. It appears that the predicted normal stresses along the middle-thickness line are least accurate, as compared to the neutron diffraction measurements (Fig. 13b). In particular, the model predicted higher compressive stress than the measurement. Moreover, the predicted tensile stresses span wider than the measured stresses. Nevertheless, the predictions for stresses on the top and bottom agree well with the measurements. The transverse stress has lowest magnitude among the three stress components (Figs. 12 and 13) and the accuracy of the prediction is deemed satisfactory, as shown in Fig. 13c, given that neutron diffraction measurement is susceptible to random errors for low stresses.

Fig. 14 shows the comparison of predicted longitudinal residual stresses between the three restraint conditions considered in the weld model. Negligible difference in stress distribution is observed for different restraints, except some fine features in the contour maps (Fig. 14a-c) and line plots (Fig. 14d). Similar negligible difference was also found for the predicted normal and transverse stresses (not shown here). However, the difference in deformed configuration is notable, i.e., the absence of restraint led to an underfill defect in the EB weld, as shown in Fig. 14a, whereas the full restraint and tack-weld restraint avoided such a defect (Fig. 14b and 14c).

For the tack-weld restraint, it is important to know the stresses that are experienced by the tack weld during welding, since there is a risk in breaking the tack weld if excessive tensile stress is present. The consequence of the potential failure of the tack weld can lead to defects in the EB weld or even failure of the EB welding process due to its tight tolerance of gap [1]. Fig. 15 shows the transverse stress distribution on the weld centre plane, focusing on the tack weld and its contiguous region near the EB weld stop end (Fig. 3c) where the transverse or out-of-plane displacement is restrained. It is clearly seen that tensile stress increases when the heat source approaches the tack weld (Fig. 15a-e) and the peak tensile stress exceeds 800 MPa (Fig. 15e). Nevertheless, the concentration of tensile stress at the tack weld disappears when the EB weld
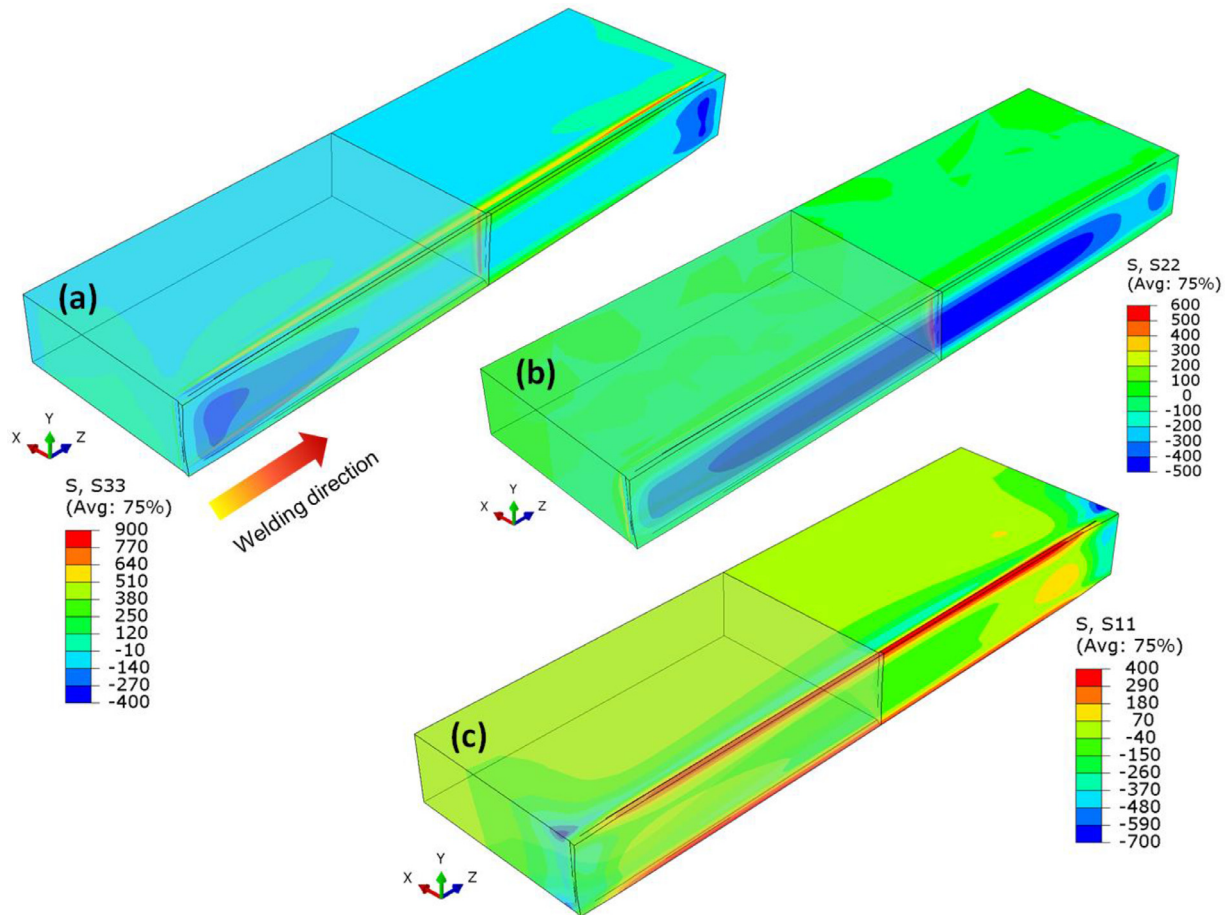
Fig. 11. 3D distributions of longitudinal (a), normal (b) and transverse (c) residual stresses that were predicted when full restraint on the weld centre plane was applied (Fig. 3a). Note that the half volume near the weld start end is set as translucent to facilitate visualisation. In the contours, averaging elements output at nodes is performed only when relative difference is less than 75% (i.e., Avg: 75%).

Table 5
Peak transverse tensile stress (MPa) at/near weld stop end at each stage of EB welding.

Welding stage	5/18 welded	9/18 welded	13/18 welded	17/18 welded
Tack-weld restraint	102	378	704	827
Full restraint	2	29	140	608

is just completed throughout the plate length (Fig. 15f). It should be noted that, although the cohesive elements representing the tack weld are assumed elastic (Section 2.2.4), the stress level is limited by the yield stress of the base material that is bonded to the cohesive elements. The actual strength of the tack weld depends on the tack welding process employed. Also note that a width of 4 mm for tack weld was adopted in the model. The actual size of the tack weld also depends on the tack welding process employed. In an extreme case, if the tack weld possesses higher strength than the base material and spans the whole EB weld centre plane, it is equivalent to the modelled full restraint condition (Fig. 3a). Fig. 16 shows the transverse stress evolution for the full restraint. It is found that the peak tensile stress at each stage of the welding is much lower for the full restraint (Fig. 16) than for the tack-weld restraint (Fig. 15), as shown in Table 5.

4. Discussion

The 3D thermal-metallurgical-mechanical model provides comprehensive information about the temperature, micro-constituents, hardness, distortion and stresses for the 30-mm thick SA508 Grade 4N steel EB weld plate. The modelling results are in good agreement with the ex-

perimental results (Figs. 2, 4–7, 12 and 13), demonstrating the achieved accuracy of the EB weld model. Although the thermal-metallurgical behaviour is not the focus of this study, accurate predictions of temperature and SSPT lay a firm basis for the subsequent mechanical analysis to gain new insights into the development of distortion and stress during the EB welding.

In recent years, EB welding has attracted increasing interest for applications in the nuclear energy industry [2,3,5,22], partly because it can minimise the weld-induced distortion which is a critical issue facing large structure manufacture [1,59]. However, the low distortion promised by EB welding is still subject to the condition that proper restraint must be applied. Our modelling results demonstrated that transverse displacement up to 0.95 mm in the half plate, equivalent to a 1.9 mm gap owing to symmetry, was generated during welding in the SA508 Grade 4N steel plate, when no restraint on the weld centre plane was applied (Fig. 8 and Fig. 9). The potential opening gap developed during EB welding can compromise the quality of the final weld and even can cause failure of the welding process. For instance, the opening gap during the EB welding without restraint caused underfill defect in the weld (Fig. 14a). Indeed, it was observed in experiments that under-
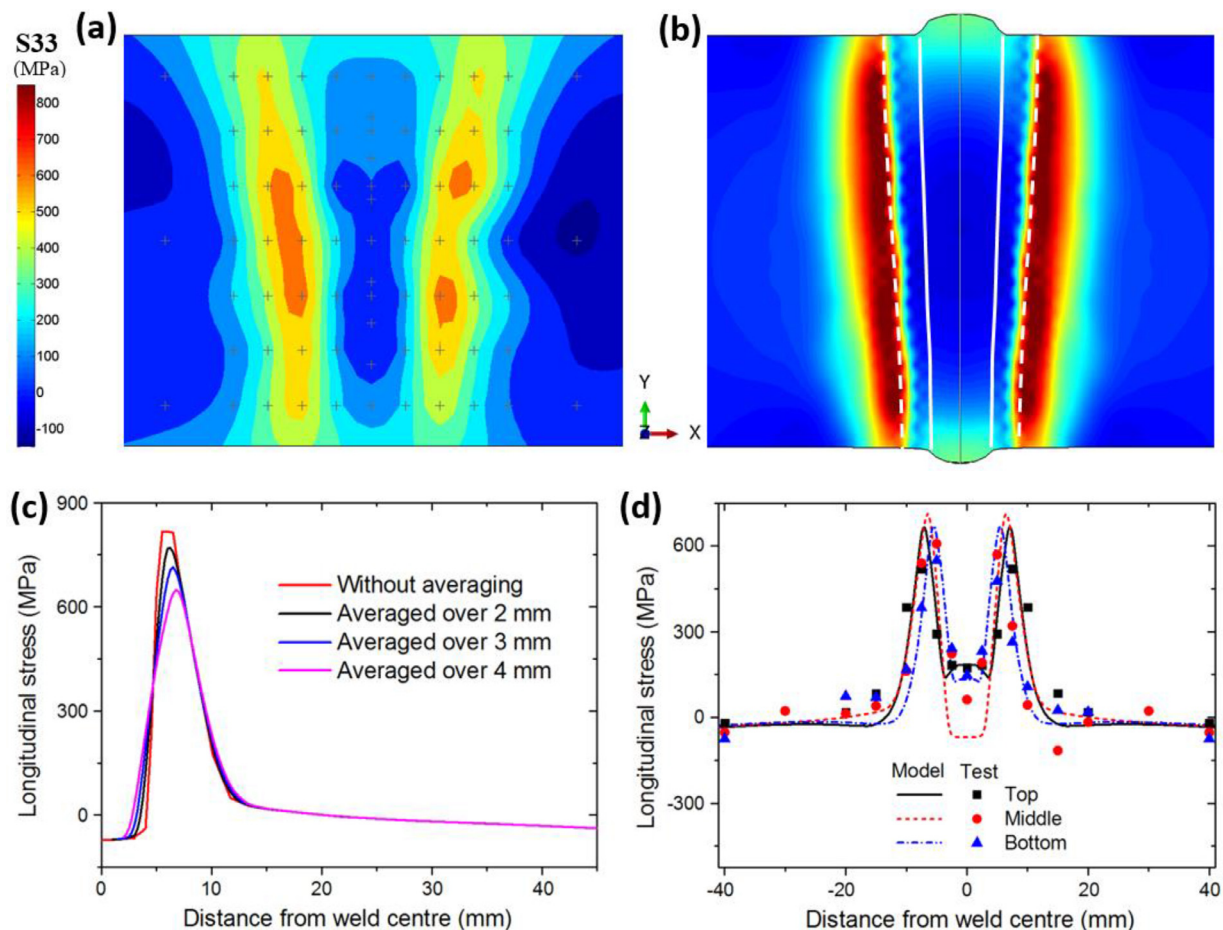
Fig. 12. (a) Contour map of longitudinal residual stress on mid-length section, as measured by neutron diffraction method; (b) contour map of predicted longitudinal residual stress (the results are mirrored and the solid and dashed lines indicate the predicted FZ and HAZ boundaries, respectively); (c) effect of data averaging on predicted stress distribution along mid-thickness path; (d) comparison between line profiles of predicted and measured longitudinal residual stresses (averaged over every 3 mm). Full restraint (Fig. 3a) was adopted in the modelling.

fill and undercut developed near the stop end of an EB weld manufactured in an 80 mm thick SA508 steel plate due to the breakage of the tack-weld restraint at the EB weld stop end [51]. It is recognised that EB welding is sensitive to the gap along the beam travelling path and a gap above 0.1 mm may not be tolerated [1], although the tolerance could be relaxed if the beam is defocused or oscillated. However, the autogenous nature of EB welding means that a gap ahead of the beam is always detrimental. EB welding cannot be stable with the presence of a gap which disturbs the keyhole and requires additional material to fill in. Fortunately, the opening gap can be largely mitigated when effective restraint is placed on the weld centre plane (Fig. 8), which, however, is at the cost of restraint-induced stresses.

When tack welds were added at the two ends of the plate to restrain the closely facing parts from separation (Fig. 3c and 3d), high out-of-plane tensile stress over 800 MPa developed at the tack weld near the EB weld stop end (Fig. 15). The modelling results show that the peak of the tensile stress was reached when the beam moved close to the tack weld (Fig. 15e), presumably because the restraint force is enhanced with reducing the distance between the tack weld and the EB, given that similar bending moment is needed to overcome the potential opening gap. The attainment of peak tensile stress indicates the critical moment that the tack weld is susceptible to failure. The loss of restraint due to the failure of tack weld will enable the inter-part gap development and hence should be avoided. The model predicted much lower tensile stress for the full restraint than for the tack-weld restraint (Figs. 15 and 16, Table 5).

Additional simulations were conducted to examine the effects of the number and width of tack welds on the restraint-induced stresses, as shown in Fig. 17. It is interesting to see that the increase in the number of tack welds is not effective to reduce the peak tensile stress (Figs. 15e and 17a), whereas the increase in the width of tack welds can effectively lower the tensile stress (Figs. 15e and 17b). These results imply that the risk in losing restraint due to tensile-stress induced cracks can be mitigated through optimising the configuration of the applied tack-weld restraint. Hereby, a full restraint (or a continuous through-length tack weld) along the welding path is preferential over the discretely distributed restraint of tack welds, and a wider tack weld at the EB weld stop end is preferential over increasing the number of narrow tack welds. It should be noted that such a suggestion stands on the basis of restraint-induced stresses during welding, which are different from the final weld residual stresses.

The weld model predicted that the restraint condition barely affects the final residual stress state (Fig. 14). Such insensitivity can be attributed to the fact that the residual stress is mainly determined by the cooling process, before which the EB weld has been already manufactured and consequently there is no substantial difference made by the central restraint imposed before the welding. In contrast, the SSPT, specifically the martensitic transformation during cooling after EB welding (Fig. 6), significantly affects residual stress [20,26,27,60–62].

Although the temperature is heterogeneously distributed in the EB weldment (Fig. 5b), the micro-constituents are approximately homogeneous and appear to be overwhelmingly martensite in the FZ and HAZ
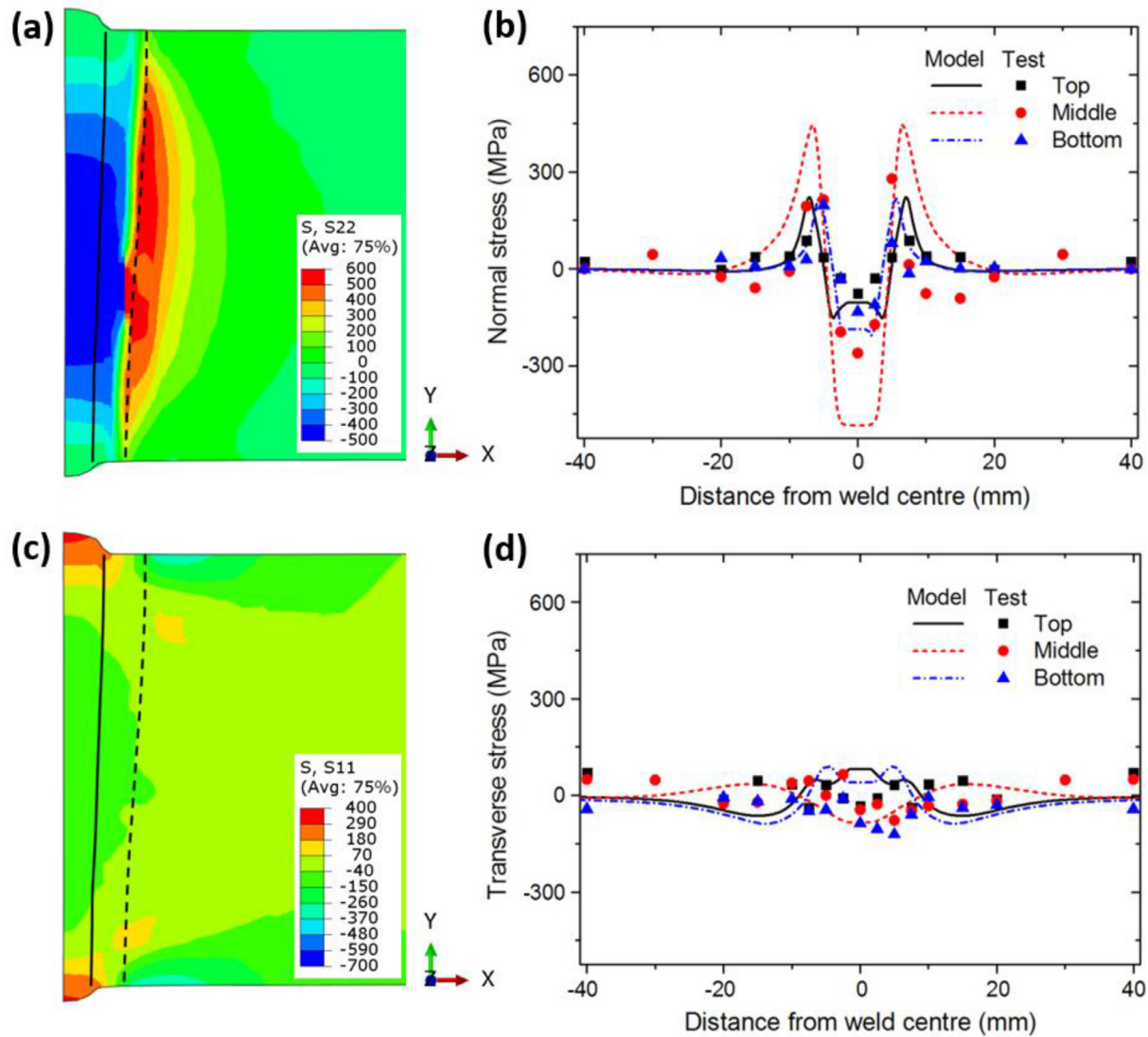
Fig. 13. Predicted normal (a) and transverse (c) residual stress contours for mid-length section, when full restraint on the weld centre plane was applied in the modelling (Fig. 3a). The line profiles of the predicted and measured normal (b) and transverse (d) residual stresses (averaged over every 3 mm for predicted stresses) are also shown. In the contours, averaging elements output at nodes is performed only when relative difference is less than 75% (i.e., Avg: 75%).

(Fig. 6). Such a microstructural feature results from the unique SSPT behaviour of the SA508 Grade 4N steel, which is prone to martensitic transformation at cooling rates typical for welding process (>10 °C/s) (Fig. 2), in contrast to the complicated SSPT behaviour of SA508 Grade 3 steel involving multiple micro-constituents [11]. The residual stresses in the FZ and HAZ tend to be less tensile and more compressive (Figs. 12 and 13), as a result of the compensation for thermal shrinkage by the martensitic transformation-induced expansion during cooling (Fig. 2b and 2c). Similar SSPT effects on residual stress have been widely observed in steel weldments involving SSPT and detailed mechanisms have been discussed in previous studies [20,26,27,60–62].

For structural integrity assessment, the sign, magnitude and distribution of weld residual stress all require careful consideration [55,63,64]. The peak tensile stress in the SA508 Grade 4N steel welded plate is located immediately outside the HAZ (Figs. 12 and 13), similar to the observations in a 30 mm thick SA508 Grade 3 steel EB weld plate [25]. However, unlike the SA508 Grade 3 steel weldment [25], the high tensile stress in the SA508 Grade 4N steel weldment is distributed in a narrow region within the base material and a steep stress gradient exists (Figs. 12 and 13). Such unique features of residual stress distribution can be attributed to the higher yield strength possessed by SA508

Grade 4N steel compared to SA508 Grade 3 steel. Unfortunately, these features pose a challenge for measuring the peak tensile stress by the neutron diffraction method, which effectively averages stresses within a gauge domain (Section 2.3). The stress averaging markedly affects the obtained peak stress (Fig. 12c).

Despite the approximate parameters for A508 Class 3 steel TIP [54] adopted in the weld model for the SA508 Grade 4N steel (Eq. 11), the accuracy of the predictions for weld residual stresses is overall good (Figs. 12 and 13). However, the compressive stress in the middle region of the FZ was overestimated by the weld model (Figs. 12 and 13). As the TIP can reduce the compressive stress in the FZ of an SA508 steel EB weld [25], it is surmised that the overestimation of the compressive stress in the FZ is likely due to the underestimation of TIP deformation. In the present dilatometry tests (Fig. 2), the samples were subjected to thermal cycles without applied load. However, the measured dilatation curves were not closed after cooling and considerable residual compressive strain was observed (Fig. 2b and 2c); in other words, the net expansion due to austenite-to-martensite transformation was larger in the model than in the experiment (Fig. 2b and 2c). The unusual residual compressive strain after returning to original temperature may involve complicated effects of back stress on TIP (e.g. nonuniform microscopic
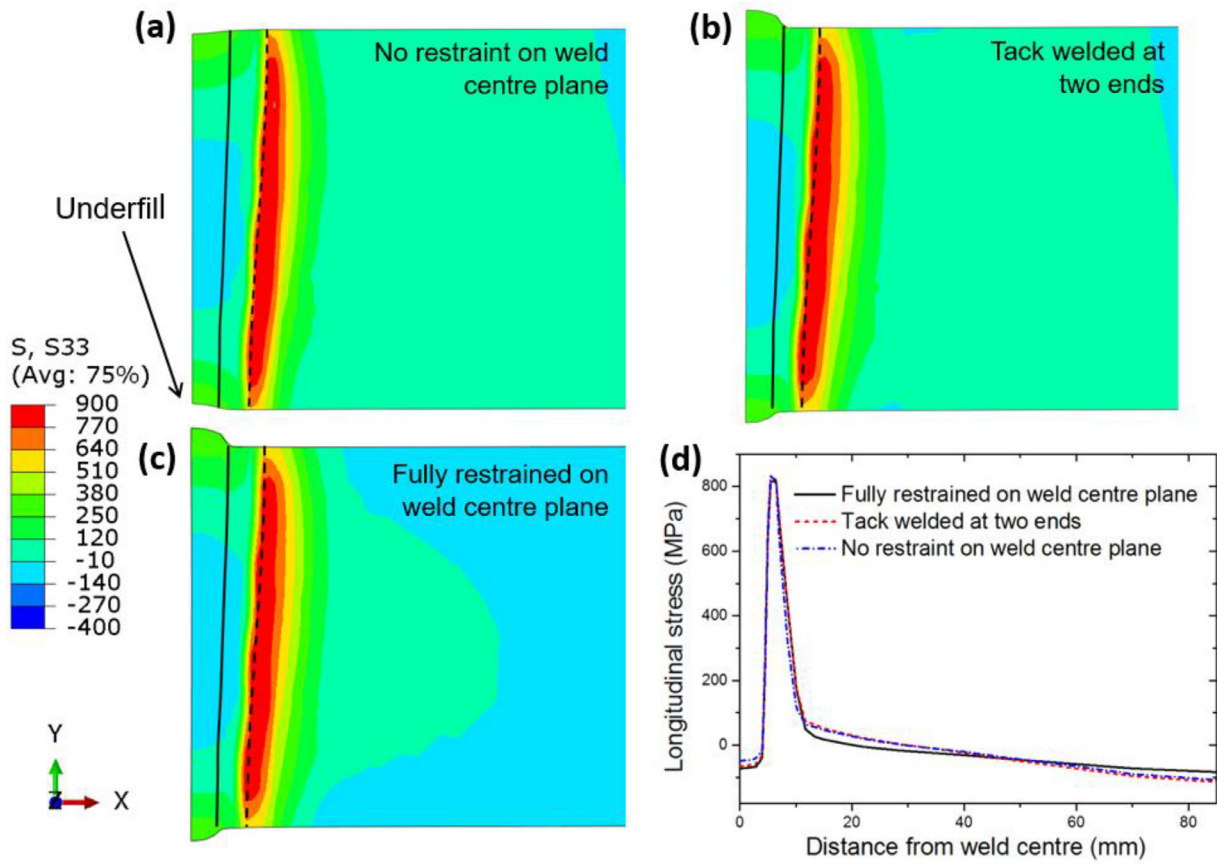
Fig. 14. Comparison between predicted longitudinal residual stress distributions on mid-length section for different restraint conditions on the weld centre plane: (a) no restraint; (b) tack-weld restraint; (c) full restraint. The line profiles of stress distributions along the mid-thickness path are shown in (d). In the contours, averaging elements output at nodes is performed only when relative difference is less than 75% (i.e., Avg: 75%).
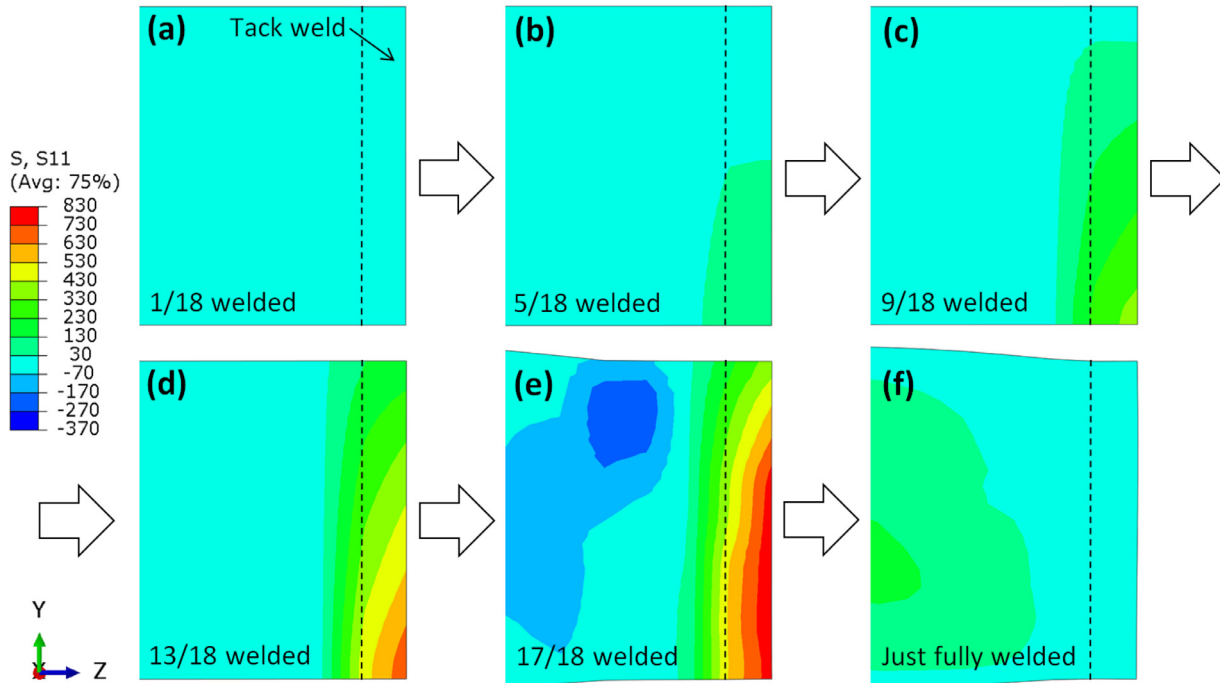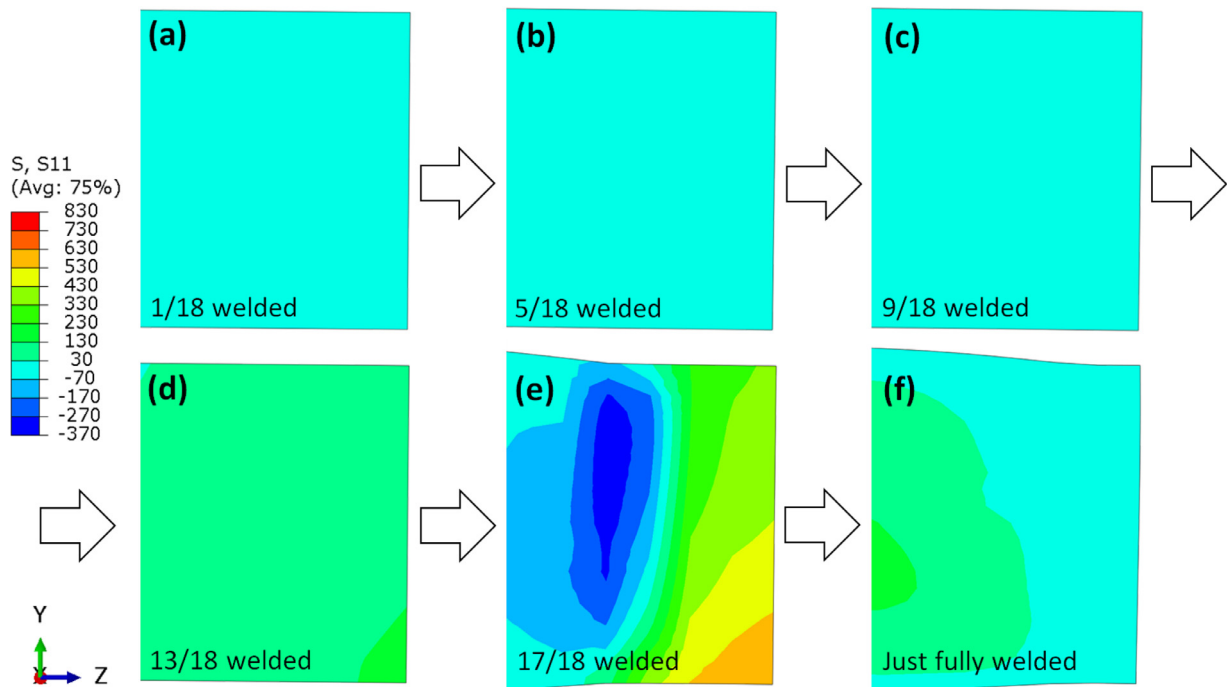

Fig. 15. Predicted evolution of the transverse stress near/within the tack weld located at the stop end of the EB weld under tack-weld restraint (Fig. 3c), when heat source travelled over: (a) 1/18 length; (b) 5/18 length; (c) 9/18 length; (d) 13/18 length; (e) 17/18 length; (f) full length (just completion of welding before cooling). In the contours, averaging elements output at nodes is performed only when relative difference is less than 75% (i.e., Avg: 75%).
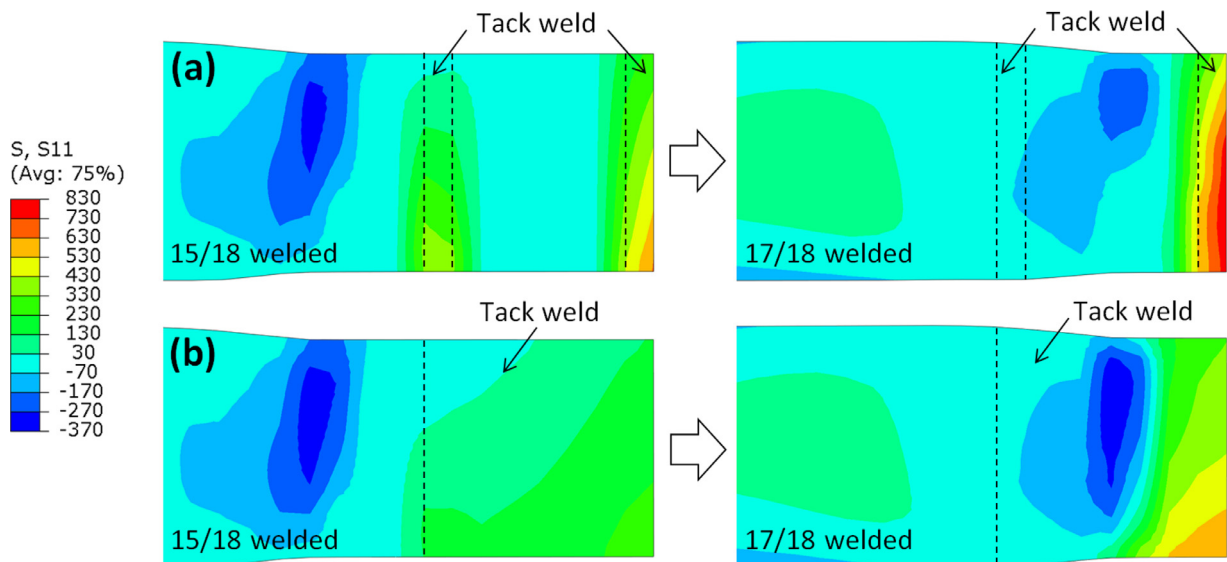
Fig. 16. Predicted evolution of the transverse stress near the stop end of the EB weld under full restraint (Fig. 3a), when heat source travelled over: (a) 1/18 length; (b) 5/18 length; (c) 9/18 length; (d) 13/18 length; (e) 17/18 length; (f) full length (just completion of welding before cooling). In the contours, averaging elements output at nodes is performed only when relative difference is less than 75% (i.e., Avg: 75%).

Fig. 17. Predicted evolution of the transverse stress of the EB weldment under different restraint conditions at the weld stop end: (a) two narrow tack welds; (b) one wide tack weld. In the contours, averaging elements output at nodes is performed only when relative difference is less than 75% (i.e., Avg: 75%).

transformation plasticity) that can occur even without applied load [48]. Future work may be devoted to improving the prediction accuracy for residual stresses using a more sophisticated TIP model that is capable of capturing the effects of back stress associated with material history. Furthermore, additional dilatometry tests on loaded samples for the specific SA508 Grade 4N steel are also needed to support the development of the new constitutive model.

5. Concluding remarks

Electron beam welding in SA508 Grade 4N steel has been modelled for a 30 mm thick plate. The predictions for temperature, micro-

constituents, hardness and residual stresses are in good agreement with experimental measurements. The validated EB weld model was further used to examine the effects of welding restraint conditions on weld-induced distortion and stresses. Main conclusions are drawn as follows:

- A marked gap develops ahead of the heat source during EB welding without restraint, accompanied by the transverse expansion of the plate and potential defects such as underfill. The opening gap is mitigated by tack-weld restraint at the weld plate ends and is eliminated by full restraint on the weld centre plane. The end tack-weld restraint leads to slightly more transient expansion and less final shrinkage than full restraint.

- High tensile stress is generated at the tack weld when the heat source approaches the EB weld stop end, potentially causing failure of the tack weld. Increasing the width of the tack weld can effectively reduce the tensile stress, while increasing the number of narrow tack welds hardly affects the peak tensile stress. Full restraint (equivalent to a continuous tack weld throughout the welding path) reduces the restraint-induced tensile stress and thereby lowers the risk in loss of restraint and the consequent welding defects.

- Martensite is a dominant transformation product in the FZ and HAZ, giving rise to elevated hardness which is approximately uniformly distributed in the FZ and HAZ. The martensitic transformation has significant implications for the sign and distribution of EB weld residual stresses.

- The most prominent feature of the residual stress distribution is that high tensile stress is located in a narrow region immediately outside the HAZ and there is a sharp increase in tensile stress across the HAZ boundary towards the base material. The residual stresses in the FZ and HAZ tend to be less tensile and more compressive, as a result of the effect of martensitic transformation. The applied restraint condition on the weld centre plane has little effect on the predicted residual stresses, since the final stress state is mainly determined by the cooling process before which the EB weld has been already manufactured to restrain the opposing parts from separation.

CRediT authorship contribution statement

Declaration of Competing Interest

The authors have no conflict of interest to declare.

Acknowledgements

References

[1] Węglowski MS, Błacha S, Phillips A. Electron beam welding – Techniques and trends – Review. Vacuum 2016;130:72–92.

[2] Sanderson A, Punshon CS, Russell JD. Advanced welding processes for fusion reactor fabrication. Fusion Eng Des 2000;49:77–87.

[3] Punshon CS. Reduced pressure electron beam welding in the power generation industry. Sixth international EPRI conference; 2004.

[4] Javadi Y, Smith MC, Abburi Venkata K, Naveed N, Forsey AN, Francis JA, Ainsworth RA, Truman CE, Smith DJ, Hosseinzadeh F, Gungor S, Bouchard PJ, Dey HC, Bhaduri AK, Mahadevan S. Residual stress measurement round robin on an electron beam welded joint between austenitic stainless steel 316L(N) and ferritic steel P91. Int J Press Vessels Pip 2017;154:41–57.

[5] Smith MC, Vasileiou AN, Rathod DW, Francis J, Irvine N, Sun Y. A review of welding research within the new nuclear manufacturing (NNUMAN) programme. In: Proceedings of ASME 2017 Pressure Vessels and Piping Conference, Hawaii, USA; 2017.

[6] Feng JC, Rathod DW, Roy MJ, Francis JA, Guo W, Irvine NM, Vasileiou AN, Sun YL, Smith MC, Li L. An evaluation of multipass narrow gap laser welding as a candidate process for the manufacture of nuclear pressure vessels. Int J Press Vessels Pip 2017;157:43–50.

[7] Shono S, Kawaguchi S, Sugino M, Nakajima N. Application of new welding technology for the manufacturing of nuclear pressure vessels. In: Design & Analysis. Elsevier; 1989. p. 1279–86.

[8] Maurer W, Ernst W, Rauch R, Kapl S, Pohl A, KrÜssel T, Vallant R, Enzinger N. Electron Beam Welding Of Atmcp Steel With 700 Mpa Yield Strength. Weld World 2012;56:85–94.

[9] Elliott S. Electron beam welding of C–Mn steels–toughness and fatigue properties. Weld. J. 1984;63:8.

[10] Zhang G, Yang X, He X, Li J, Hu H. Enhancement of mechanical properties and failure mechanism of electron beam welded 300M ultrahigh strength steel joints. Mater Des. 2013;45:56–66.

[11] Obasi G, Pickering EJ, Vasileiou AN, Sun YL, Rathod D, Preuss M, Francis JA, Smith MC. Measurement and prediction of phase transformation kinetics in a nuclear steel during rapid thermal cycles. Metall Mater Trans A 2019;50:1715–31.

[12] Yang Z, Liu Z, He X, Qiao S, Xie C. Effect of microstructure on the impact toughness and temper embrittlement of SA508Gr.4N steel for advanced pressure vessel materials. Sci Rep 2018;8:207.

[13] Flint TF, Francis JA, Smith MC, Vasileiou AN. Semi-analytical solutions for the transient temperature fields induced by a moving heat source in an orthogonal domain. Int J Therm Sci 2018;123:140–50.

[14] Huang B, Chen X, Pang S, Hu R. A three-dimensional model of coupling dynamics of keyhole and weld pool during electron beam welding. Int J Heat Mass Transf 2017;115:159–73.

[15] Withers PJ, Bhadeshia HKDH. Residual stress. Part 2 – Nature and origins. Mater Sci Technol 2001;17:366–75.

[16] Hemmesi K, Mallet P, Farajian M. Numerical evaluation of surface welding residual stress behavior under multiaxial mechanical loading and experimental validations. Int J Mech Sci 2020;168:105127.

[17] Salerno G, Bennett C, Sun W, Becker A, Palumbo N, Kelleher J, Zhang SY. On the interaction between welding residual stresses: A numerical and experimental investigation. Int J Mech Sci 2018;144:654–67.

[18] Ha J, Huh H. Failure characterization of laser welds under combined loading conditions. Int J Mech Sci 2013;69:40–58.

[19] Withers P. Residual stress and its role in failure, Reports on progress in physics 2007;70:2211.

[20] Francis JA, Bhadeshia HKDH, Withers PJ. Welding residual stresses in ferritic power plant steels. Mater Sci Technol 2007;23:1009–20.

[21] Withers P, Turski M, Edwards L, Bouchard P, Buttle D. Recent advances in residual stress measurement. Int J Press Vessels Pip 2008;85:118–27.

[22] Rathod DW, Francis JA, Vasileiou AN, Roy MJ, English PD, Balakrishnan J, Smith MC, Irvine NM. Residual stresses in arc and electron-beam welds in 130 mm thick SA508 steel: Part 1 - Manufacture. Int J Press Vessels Pip 2019;172:313–28.

[23] Vasileiou AN, Smith MC, Francis JA, Rathod DW, Balakrishnan J, Irvine NM. Residual stresses in arc and electron-beam welds in 130 mm thick SA508 steel: Part 2 –measurements. Int J Press Vessels Pip 2019;172:379–90.

[24] Balakrishnan J, Vasileiou AN, Francis JA, Smith MC, Roy MJ, Callaghan MD, Irvine NM. Residual stress distributions in arc, laser and electron-beam welds in 30 mm thick SA508 steel: A cross-process comparison. Int J Press Vessels Pip 2018;162:59–70.

[25] Vasileiou AN, Smith MC, Balakrishnan J, Francis JA, Hamelin CJ. The impact of transformation plasticity on the electron beam welding of thick-section ferritic steel components. Nucl Eng Des 2017;323:309–16.

[26] Hamelin CJ, Muránsky O, Smith MC, Holden TM, Luzin V, Bendeich PJ, Edwards L. Validation of a numerical model used to predict phase distribution and residual stress in ferritic steel weldments. Acta Mater 2014;75:1–19.

[27] Dai H, Francis J, Stone H, Bhadeshia H, Withers P. Characterizing phase transformations and their effects on ferritic weld residual stresses with X-rays and neutrons. Metall Mater Trans A 2008;39:3070–8.

[28] Rong Y, Lei T, Xu J, Huang Y, Wang C. Residual stress modelling in laser welding marine steel EH36 considering a thermodynamics-based solid phase transformation. Int J Mech Sci 2018;146-147:180–90.

[29] Cheon J, Na S-J. Prediction of welding residual stress with real-time phase transformation by CFD thermal analysis. Int J Mech Sci 2017;131-132:37–51.

[30] Ni J, Wang X, Gong J, Wahab MA. A multi-phase model for transformation plasticity using thermodynamics-based metallurgical algorithm. Int J Mech Sci 2018;148:135–48.

[31] Rathod DW, Francis JA, Roy MJ, Obasi G, Irvine NM. Thermal cycle-dependent metallurgical variations and their effects on the through-thickness mechanical properties in thick section narrow-gap welds. Mater Sci Eng 2017;707:399–411.

[32] Wang Q, Liu XS, Wang P, Xiong X, Fang HY. Numerical simulation of residual stress in 10Ni5CrMoV steel weldments. J Mater Process Technol 2017;240:77–86.

[33] Lindgren L-E. Computational welding mechanics. Elsevier; 2014.

[34] Bendeich PJ, Smith MC, Carr DG, Edwards L. Sensitivity of predicted weld residual stresses in the NeT Task Group 1 single bead on plate benchmark problem to finite element mesh design and heat source characteristics. In: ASME 2009 Pressure Vessels and Piping Conference. American Society of Mechanical Engineers; 2009. p. 501–7.

[35] Flint TF, Francis JA, Smith MC, Balakrishnan J. Extension of the double-ellipsoidal heat source model to narrow-groove and keyhole weld configurations. J Mater Process Technol 2017;246:123–35.

[36] Smith R. FEAT-WMT: Weld-modelling tool user guide. FeatPlus Limited; 2018.

[37] Li MV, Niebuhr DV, Meekisho LL, Atteridge DG. A computational model for the prediction of steel hardenability. Metall. Mater. Trans. B 1998;29:661–72.

[38] Sun YL, Obasi G, Hamelin CJ, Vasileiou AN, Flint TF, Balakrishnan J, Smith MC, Francis JA. Effects of dilution on alloy content and microstructure in multi-pass steel welds. J Mater Process Technol 2019;265:71–86.

[39] Sun YL, Obasi G, Hamelin CJ, Vasileiou AN, Flint TF, Francis JA, Smith MC. Characterisation and modelling of tempering during multi-pass welding. J Mater Process Technol 2019;270:118–31.

[40] Sun YL, Hamelin CJ, Flint TF, Vasileiou AN, Francis JA, Smith MC. Prediction of dilution and its impact on the metallurgical and mechanical behavior of a multipass steel weldment. J Pressure Vessel Technol 2019;141.

[41] Leblond JB, Devaux J. A new kinetic model for anisothermal metallurgical transformations in steels including effect of austenite grain size. Acta Metall 1984;32:137–46.

[42] Sun YL, Hamelin CJ, Flint TF, Xiong Q, Vasileiou AN, Pantelis I, Francis JA, Smith MC. Multi-pass ferritic steel weld modelling: Phase transformation and residual stress. In: Sommitsch C, Enzinger N, Mayr P, editors. Mathematical modelling of weld phenomena, 12. Verlag der Technischen Universität Graz; 2019. p. 149–66.

[43] Pous-Romero H, Lonardelli I, Cogswell D, Bhadeshia HKDH. Austenite grain growth in a nuclear pressure vessel steel. Mater. Sci. Eng. 2013;567:72–9.

[44] Kirkaldy J, Venugopalan D. Prediction of microstructure and hardenability in low-alloy steels. Phase Transf Ferr Alloys 1983;125:148.

[45] Koistinen DP, Marburger RE. A general equation prescribing the extent of the austenite-martensite transformation in pure iron-carbon alloys and plain carbon steels. Acta Metall 1959;7:59–60.

[46] O'Meara N, Abdolvand H, Francis JA, Smith SD, Withers PJ. Quantifying the metallurgical response of a nuclear steel to welding thermal cycles. Mater Sci Technol 2016;32:1517–4532.

[47] Pickering EJ, Collins J, Stark A, Connor LD, Kiely AA, Stone HJ. In situ observations of continuous cooling transformations in low alloy steels. Mater Charact 2020;165:110355.

[48] Nagayama K, Terasaki T, Tanaka K, Fischer FD, Antretter T, Cailletaud G, Azzouz F. Mechanical properties of a Cr–Ni–Mo–Al–Ti maraging steel in the process of martensitic transformation. Mater Sci Eng 2001;308:25–37.

[49] J. Priest, EBW of SA508 Grade 4N 30mm Plates (Report NO. NIN441-RP01-01), in, Nuclear-AMRC, 2016.

[50] Pirondi A, Bonora N, Steglich D, Brocks W, Hellmann D. Simulation of failure under cyclic plastic loading by damage models. Int J Plast 2006;22:2146–70.

[51] Smith MC, Sun YL, Akrivos V, Vasileiou AN, Pickering EJ, Irvine NM, Carruthers A, Collins J. In: Electron beam welding in SA608 Grade 4N and Grade 3 Class 1 thick–section steels; 2019. p. 194.

[52] Smith M, Bouchard P, Turski M, Edwards L, Dennis R. Accurate prediction of residual stress in stainless steel welds. Comput Mater Sci 2012;54:312–28.

[53] Muránsky O, Hamelin C, Smith M, Bendeich P, Edwards L. The effect of plasticity theory on predicted residual stress fields in numerical weld analyses. Comput Mater Sci 2012;54:125–34.

[54] Leblond J-B, Mottet G, Devaux J, Devaux J-C. Mathematical models of anisothermal phase transformations in steels, and predicted plastic behaviour. Mater Sci Technol 1985;1:815–22.

[55] EDF Energy, R6: Assessment of the integrity of structures containing defects, in: Revision 4, with amendments to Amendment 11, Gloucester, (2015).

[56] Bate S, Smith M. Determination of residual stresses in welded components by finite element analysis. Mater Sci Technol 2016;32:1505–16.

[57] Maynier P, Dollet J, Bastien P. Creusot-Loire system for the prediction of the mechanical properties of low alloy steel products. In: Doane DV, Kirkaldy JS, editors. Hardenability concepts with applications to steels. ,: The Metallurgical Society of AIME; 1978. p. 518–45.

[58] Price JWH, Ziara-Paradowska A, Joshi S, Finlayson T, Semetay C, Nied H. Comparison of experimental and theoretical residual stresses in welds: the issue of gauge volume. Int J Mech Sci 2008;50:513–21.

[59] Smith DJ, Zheng G, Hurrell PR, Gill CM, Pellereau BME, Ayres K, Goudar D, Kingston E. Measured and predicted residual stresses in thick section electron beam welded steels. Int J Press Vessels Pip 2014;120-121:66–79.

[60] Deng D, Murakawa H. Influence of transformation induced plasticity on simulated results of welding residual stress in low temperature transformation steel. Comput Mater Sci 2013;78:55–62.

[61] Ooi SW, Garnham JE, Ramjaun TI. Review: low transformation temperature weld filler for tensile residual stress reduction. Mater Des 2014;56:773–81.

[62] Taljat B, Radhakrishnan B, Zacharia T. Numerical analysis of GTA welding process with emphasis on post-solidification phase transformation effects on residual stresses. Mater Sci Eng 1998;246:45–54.

[63] James MN. Residual stress influences on structural reliability. Eng Fail Anal 2011;18:1909–20.

[64] Bouchard PJ. Code characterisation of weld residual stress levels and the problem of innate scatter. Int J Press Vessels Pip 2008;85:152–65.